

AD-A264 465



2

DARPA/ONR Grant #N00014-91-J-1976

Seventh Quarterly Progress Report
(covering the period of 02/01/93 - 04/30/93)

Project Title: Development of Ultra-Low Noise, High Sensitivity Planar Metal Grating Coupled III-V Multiquantum Well Infrared Detectors for Focal Plane Array Staring IR Sensor Systems

Submitted to

S DTIC
ELECTE **D**
MAY 20 1993
A

Max N. Yoder
Office of Naval Research
Code 1114 SS
800 North Quincy Street
Arlington, VA 22217-5000

Prepared by

Sheng S. Li
Professor

Dept. of Electrical Engineering
University of Florida
Gainesville, Florida 32611

Tel.(904)-392-4937
Fax(904)-392-8671

This document has been approved
for public release and sale; its
distribution is unlimited.

May 1, 1993

93-11256



3 3 5

Seventh Quarterly Progress Report:02/1/93 - 04/30/93

Project Title: Development of ultra-low noise high-detectivity planar metal grating coupled III-V multiquantum-well/superlattice barrier infrared photodetectors for focal plane array (FPA) staring infrared sensor systems.

Program Manager: Max N. Yoder, Office of Naval Research, Code 1114SS, Arlington, VA.

Principal Investigator: Sheng S. Li, Professor, University of Florida, Gainesville, FL.

Project Objectives:

1. To develop ultra-low dark current and high detectivity planar metal grating coupled bound-to-miniband (BTM) III-V quantum well infrared photodetectors (QWIPs) for 8 to 12 μm focal plane arrays (FPAs) staring IR sensor systems.
2. To develop novel type-I and type-II III-V QWIPs with multicolor, broad and narrow band spectral response in the 8 to 14 μm wavelength range. The material systems to be studied include GaAs/AlGaAs, AlAs/AlGaAs, InGaP/GaAs (by MOCVD) grown on GaAs substrates, and InAlAs/InGaAs (MBE) grown on InP substrate.
3. To conduct theoretical and experimental studies of the planar metal grating coupled structures for normal incidence illumination on QWIPs. Different metal grating coupled structures using 1-D (line) and 2-D (square mesh and dot) metal gratings will be studied in order to achieve high coupling quantum efficiency under normal frontside and backside illuminations on QWIPs.
4. To perform theoretical and experimental studies of dark current, photocurrent, optical absorption, spectral responsivity, noise, and detectivity in different types of QWIPs developed under this program.

	<input checked="" type="checkbox"/>
	<input type="checkbox"/>
	<input type="checkbox"/>
per ltr.	
	Activity Code
	Result and/or Spectral
A-1	

I. Introduction

During this reporting period (02-01-93 to 04-30-93) we have continued to make excellent progress towards the program goals. We have continue to design, fabricate, and characterize new types of metal grating coupled n-type GaAs/AlGaAs, AlAs/AlGaAs, InAlAs/InGaAs, and InGaP/GaAs QWIPs for 2 - 14 μm focal plane arrays (FPAs) staring infrared sensor applications. In addition, a new normal incidence two-color p-type strained layer InGaAs/InAlAs QWIP has been developed for the first time with highest detectivity and low dark current reported for p-type QWIPs. Specific tasks performed during this period include: (i) design, growth, and fabrication of a new normal incidence p-type strained InGaAs/InAlAs QWIP grown on InP substrate by MBE technique, (ii) design, growth, and fabrication of a new multi-color enhanced bound-to-continuum band (EBTC) and bound-to-miniband (BTM) transition GaAs/GaInP QWIPs grown on GaAs substrate by using MOCVD technique, (iii) completed theoretical and experimental studies of four dual mode operation QWIPs fabricated from GaAs/AlGaAs, InGaAs/InAlAs, and AlAs/AlGaAs material systems, (iv) completed the theoretical and experimental studies of the type-II AlAs/AlGaAs QWIP, (v) applied a new 2-D square mesh grating coupler structure to an InAlAs/InGaAs BTM QWIP which shows a significant improvement in detector's responsivity and detectivity, (vi) performed noise characterization of an InGaAs/InAlAs BTM QWIP and identified the noise sources in the QWIP, (vii) completed numerical simulations of coupling quantum efficiency versus grating periodicity and size for a two-dimensional (2-D) double-period square mesh metal grating coupler for use in both the standard and BTM QWIPs. Detailed research accomplishments and publications are given in Section II. The technical results are discussed in Section III.

II. Research Accomplishments and Publications

Research accomplishments and publications during this period are summarized as follows:

2.1 Research Accomplishments:

1. A new normal incident p-type strained InGaAs/InAlAs QWIP for two-color ($\lambda_p = 7.8$ and $10.8 \mu\text{m}$) has been demonstrated for the first time. The detectivities at both wavelengths are given by 1.5×10^9 and $3.6 \times 10^9 \text{ cm} - \text{Hz}^{1/2}/\text{W}$, at $V = 6 \text{ V}$ and $T = 77 \text{ K}$, respectively. These are the high values ever reported for a p-type III-V QWIP. The dark current is very low and shows symmetry property under forward and reverse bias conditions. The preliminary results of this QWIP are depicted in Section 3.1.

2. A comparison of four III-V quantum well infrared photodetectors (QWIPs) operating in the photoconductive (PC) and photovoltaic (PV) detection modes for multicolor detection in the wavelength range from 2 to 14 μm is given in Section 3.2. These dual-mode operation QWIPs were grown by the MBE technique using GaAs/AlGaAs and AlAs/AlGaAs and InGaAs/InAlAs material systems. Based on the bound-to-miniband (BTM) and enhanced bound-to-continuum (EBTC) intersubband transition schemes, these QWIPs offer large optical absorption, low dark current, and high detectivity for use in the large area IR focal plane array image sensor applications.
3. A detailed analysis of the normal incidence type-II indirect AlAs/Al_{0.5}Ga_{0.5}As QWIP grown on (110) GaAs by MBE technique for the mid- and long- wavelength multicolor IR detection has been carried out. The normal incident excitation of long wavelength intersubband transition was achieved in the [110] X-band confined AlAs quantum wells. Six absorption peaks including four from the X-band to Γ -band intersubband resonant transitions were observed at wavelengths, $\lambda_{p1-6} = 2.2, 2.7, 3.5, 4.8, 6.5$ and $12.5 \mu\text{m}$. The resonant transport from X-band to Γ -band gives rise to high photoconductive gain, which is highly desirable for focal plane arrays (FPAs) image sensor applications. The results are presented in Section 3.3.
4. Design, fabrication, and characterization of 2-D square mesh grating couplers formed on a BTM transition In_{0.52}Al_{0.48}As/In_{0.53}Ga_{0.47}As QWIP have been carried out. The results showed a significant improvement in the responsivity for a 2-D square mesh grating coupled InGaAs BTM QWIP. Coupling quantum efficiency $\eta \sim 29\%$ was obtained for this QWIP under normal incidence backside illumination at $\lambda_p = 10 \mu\text{m}$. Details of the results are discussed in Section 3.4.
5. The effects of grating size and shape variation on the photoresponse of a 2-D square mesh metal grating coupler for a GaAs/AlGaAs QWIP has been analyzed. In the fabrication of small grating coupler structure on QWIPs, some distortion in the aperture's shape and size may occur during processing. This may lead to nonuniformed photoresponse of cell-to-cell in the QWIP arrays. The effect can be minimized by either selecting a larger aperture size or using a larger grating period. Details are depicted in Section 3.5.
6. Performed noise characterization on an InGaAs/InAlAs BTM QWIP. From measurements of noise current as a function of the frequency (10 to 10^5 Hzs), the noise sources in this QWIP were identified. The results revealed that Johnson noise dominated in the PV mode operation QWIP while the g-r noise prevailed in the PC mode operation QWIP. In addition, the 1/f

noise was also observed in the PC mode operation QWIP under large bias voltages. Results of the noise measurements on the InGaAs/InAlAs BTM QWIP are given in Section 3.6.

7. An AASERT proposal on, "Development of a Normal Incidence High Performance p-Type Strained Layer InGaAs/InAlAs Quantum Well Infrared Photodetectors," has been selected for funding by DARPA. The proposed research is an augmented effort of the current DARPA contract on QWIPs for focal plane arrays (FPAs) applications. A new student, who has just completed MS degree from Stanford University (US citizen), has been selected to start working on this proposed topic this summer.

2.2. Refereed Journal Papers:

1. L. S. Yu and S. S. Li, "A Low Dark Current, High Detectivity Grating Coupled AlGaAs/GaAs Multiple Quantum Well IR Detector Using Bound-to-Miniband Transition for 10 μm Detection," *Appl. Phys. Letts.*, 59 (11), p.1332, Sept.9, 1991.
2. L. S. Yu, S. S. Li, and Pin Ho "Largely Enhanced Bound-to-Miniband Absorption in an InGaAs Multiple Quantum Well with a Short-Period Superlattice InAlAs/InGaAs Barrier " *Applied Phys. Letts.*, 59 (21), p.2712, Nov. 18, 1991.
3. L. S. Yu, Y. H. Wang, S. S. Li and Pin Ho, "A Low Dark Current Step-Bound-to-Miniband Transition InGaAs/GaAs/AlGaAs Multiquantum Well Infrared Detector," *Appl. Phys. Letts.* 60(8), p.992, Feb.24, 1992.
4. L. S. Yu, S. S. Li, and P. Ho, "A Normal Incident Type-II Quantum Well Infrared Detector Using an Indirect AlAs/Al_{0.5}Ga_{0.5}As System Grown on [110] GaAs," *Electronics Letts.*, 28(15) p.1468, July,16, 1992.
5. L. S. Yu, S. S. Li, Y. H. Wang, and Y. C. Kao, "A Study of Coupling Efficiency versus Grating Periodicity in A Normal Incident Grating-Coupled GaAs/AlGaAs Quantum Well Infrared Detector," *J. Appl. Phys.*, 72(6), pp.2105, Sept. 15, 1992.
6. Y. H. Wang, S. S. Li, and P. Ho, "A Photovoltaic and Photoconductive Dual Mode Operation GaAs/AlGaAs Quantum Well Infrared Detector for Two Band Detection," *Appl. Phys. Lett.*, 62(1), pp.93, Jan. 4 1993.

7. Y. H. Wang, S. S. Li, and P. Ho, "A Voltage-Tunable Dual Mode Operation InAlAs/InGaAs Bound-to-Miniband Transition QWIP for Narrow and Broad Band Detection at 10 μm ," *Appl. Phys. Lett.*, 62(6), pp.621 Feb. 8, 1993.
8. P. Ho, P. A. Martin, L. S. Yu, and S. S. Li, "Growth of GaAs and AlGaAs on Misoriented (110) GaAs and a Normal Incidence Type-II Quantum Well Infrared Detector," accepted, *J. Vacuum Science and Technology*, Oct., 1992.
9. S. S. Li, M. Y. Chuang and L. S. Yu, "Current Conduction Mechanisms in Bound-to-Miniband Transition III-V Quantum Well Infrared Photodetectors," *Semiconductor Science and Technology*, vol.8, pp.406-411, 1993.
10. Y. H. Wang, Sheng S. Li, P. Ho, and M. O. Manasreh, "A Normal Incidence Type-II Quantum Well Infrared Photodetector Using An Indirect AlAs/AlGaAs System Grown on [110] GaAs for the Mid- and Long-Wavelength Multicolor Detection," *J. Appl. Phys.*, accepted, to be published in July 15 issue, 1993.
11. Y. C. Wang and S. S. Li, "A Numerical Analysis of Double Periodic Reflection Metal Grating Coupler for Multiquantum Well Infrared Photodetectors," accepted, *J. Appl. Phys.*, April, 1993.
12. M. Y. Chuang, Y. C. Wang, C. Wang, and Sheng S. Li, "Enhancement of Responsivity in an InGaAs/InAlAs Quantum Well Infrared Photodetector by Using a 2-D Square Mesh Metal Grating Coupler," *Appl. Phys. Lett.*, submitted, March, 1993.

2.3. Workshop and Conference Presentations

1. L. S. Yu, S. S. Li, and Pin Ho, " Largely Enhanced Intra-subband Absorption in a Wide InAlAs/InGaAs Quantum Well with a Short-Period Superlattice Barrier Structure," paper presented at the *SPIE's Symposium on Quantum Wells and Superlattices*, Somerset, NJ, 23-27 March, 1992. Paper published in the SPIE Conference Proceeding.
2. S. S. Li and L. S. Yu, "Grating Coupled Bound-to-Miniband Transition III-V Quantum Well Infrared Detectors," **invited paper**, presented at *the Innovative Long Wavelength Infrared Photodetector Workshop*, Jet Propulsion Lab., Pasadena, CA, April 7-9, 1992.
3. L. S. Yu and S. S. Li, "A Normal Incident Type-II Quantum Well Infrared Detector Using an Indirect AlAs/Al_{0.5}Ga_{0.5}As System Grown on [110] GaAs, paper presented at *the Innovative*

Long Wavelength Infrared Photodetector Workshop, Jet Propulsion Lab., Pasadena, CA, April 7-9, 1992.

4. L. S. Yu, S. S. Li, Y. H. Wang, and P. Ho, "Grating Coupled III-V Quantum Well Infrared Detectors Using Bound-to-Miniband Transition," paper presented at *the SPIE Conference on Infrared Detectors and Focal Plane Arrays at OE/Aerospace Sensing 92*," Orlando, FL, April 20-24, 1992. Full paper published in the SPIE conference proceeding.
5. S. S. Li, "Grating Coupled Bound-to-Miniband Transition III-V Multiquantum Well Infrared Photodetectors," presented at the DARPA IR Detector Workshop. Washington D.C., June 12, 1992.
6. S. S. Li, M. Y. Chuang and L. S. Yu, "Current Conduction Mechanisms in Bound-to-Miniband Transition III-V Quantum Well Infrared Photodetectors," paper presented at *the International Conference on Narrow Gap Semiconductors*, University of Southampton, Southampton, UK, July 19-23, 1992.
7. P. Ho, P. A. Martin, L. S. Yu, and S. S. Li, "Growth of GaAs and AlGaAs on Misoriented (110) GaAs and a Normal Incidence Type-II Quantum Well Infrared Detector," paper presented at *the 12th North American Conference on Molecular Beam Epitaxy*," Oct. 12-14, 1992.
8. S. S. Li, "Novel Grating Coupled Miniband Transport III-V Multiquantum Well Infrared Photodetectors for Focal Plane Array Applications," presented at the DARPA IR Detector Workshop, Washington D.C., Dec 11, 1992.
9. S. S. Li, Y. H. Wang, M. Y. Chuang, P. Ho, , "Photoconductive and Photovoltaic Dual-Mode Operation III-V Quantum Well Infrared Photodetectors for 2 - 14 μm Detection," presented at the Materials Research Society (MRS), Symposium C2 on **Infrared Detectors**, San Francisco, April 12-16, 1993.
10. D. Wang, Y. H. Wang, G. Bosman and S. S. Li, "Noise Characterization of Novel Quantum Well Infrared Photodetectors," **Invited paper** to be presented at the *12th Int. Conf. on Noise in Physical Systems and 1/f Fluctuations - The High Technologies Conference*, St. Louis, MO, August 16-20, 1993.
11. Sheng S. Li, "Novel Grating Coupled III-V Quantum Well Infrared Photodetectors for Infrared Focal Plane Array Image Sensor Applications," **invited paper** to be presented at *the NATO*

Advanced Research Workshop on Intersubband Transition Physics and Devices, Whistler, Canada, September 7 - 10, 1993.

12. Sheng S. Li, "Grating Coupled III-V Quantum Well Infrared Photodetectors for Mid-Wavelength and Long-Wavelength Infrared Detection," **invited paper** to be presented at *the First International Symposium on Long Wavelength Infrared Photodetectors* in conjunction with the Fall Electrochemical Society (ECS) Meeting in New Orleans, LA, October 10 -15, 1993.

2.4 Interactions with Government and Industrial Laboratories

1. Continued to collaborate with Dr. Pin Ho of General Electric Co. in Syracuse, NY, on the growth of III-V QWIP's structures by using the molecular beam epitaxy (MBE) technique.
2. Continued to collaborate and exchange technical information on QWIP's research with Dr. Swami Swaminathan of AT & T Bell Lab., in Breinigsville, PA, on the planar metal grating coupler structure developed at the University of Florida for applications in their QWIP focal plane arrays. Dr. Li has performed simulations of coupling quantum efficiency on the 2-D grating coupled GaAs QWIPs fabricated by Bell Lab., and the results are compared their experimental data. Excellent agreement was obtained between our calculations and Bell Lab's data.
3. Dr. Li gave an invited talk at the Electronics Technology Laboratory, WRDC/ELRA, WPAFB, Ohio, on *The bound-to-miniband transition III-V QWIPs* on August 21, 92, and discussed with Dr. Omar Manasreh and his colleagues in the Electronics Technology Laboratory at the Wright Patterson Air Force Base. Dr. Manasreh had performed optical absorption measurements on Dr. Li's QWIP samples, while Dr. Li has fabricated and characterized some QWIP samples provided by Dr. Manasreh. Dr. Manasreh has asked Dr. Li to write a book chapter on miniband transport QWIP for a new monograph on long wavelength quantum well infrared photodetectors to be published by Artech Publishing Co.
4. Dr. Li was invited by the American Engineering Education Association (AEEA) to serve on a review panel for Naval Postdoctoral Fellowship program in Washington D.C. August 7, 92, to review a dozen of proposals submitted by various applicants. Dr. Li was responsible for recommending one of the applicants whose proposal was on quantum well IR detector research.

5. Dr. Li was invited by the Organization Committee of ECS to give an invited paper on Miniband QWIPs at the *first International Symposium on Long Wavelength Infrared Photodetectors* to be held in New Orleans, October 10-15, 1993.
6. Dr. Li was invited to present an invited talk of his recent work on quantum well infrared photodetectors at the NATO Advanced Research Workshop On Long Wavelength Infrared Intersubband Transition Physics and Devices, to be held in Whistler, Canada, Sept. 7-10, 1993.

III. Technical Results

3.1 A New Normal Incidence Two-color P-type Strained InGaAs/InAlAs QWIP

Quantum well infrared photodetectors (QWIPs) using n-type GaAs/AlGaAs and InGaAs/InAlAs systems for 8 - 14 μm detection have been extensively studied in recent years¹⁻². With low electron effective mass and high electron mobility, the n-type GaAs and InGaAs QWIPs offer excellent IR detection properties. However, the quantum mechanical selection rule for the intersubband transition requires that the IR radiation electric fields have a component perpendicular to the quantum well plane in order to induce intersubband absorption in the quantum wells. As a result, for focal plane arrays (FPAs) image sensor applications, the use of metal or dielectric grating structure for coupling IR radiation into the quantum wells becomes necessary to allow normal incidence illumination for the n-type QWIPs.

P-type QWIPs using intersubband transitions in the valence bands have been demonstrated³⁻⁶ recently in the lattice-matched GaAs/AlGaAs and InGaAs/InAlAs systems. Due to a strong mixing between the light holes and heavy holes, normal incident illumination is allowed for the intersubband transition in p-type QWIPs. In general, the intersubband transitions under normal incident radiation in p-type quantum wells are induced by linear combination of p-like valence-band Bloch state which provides a nonzero coupling between this component and the normal radiation field. The strong mixing between the IR radiation field and the heavy holes enhances the normal incidence intersubband absorption process. However, in the lattice-matched quantum well systems, this intersubband transition occurs between the heavy hole ground state and the upper excited states. Due to the relatively large heavy hole mass, relative weak absorption and low responsivity are expected in the IR wavelength range. If we intentionally introduce a tensile strain between the quantum well and the barrier layers, the effect of tensile strain can cause heavy-hole state and light-

hole ground state inverted. This in turn will cause the intersubband transition from the populated light-hole ground state to the upper energy band states. Since the light hole has a small effective mass (comparable to the electron effective mass), the optical absorption and the responsivity of p-type QWIPs can be greatly enhanced by using this approach.

In this section we present a new normal incidence p-type $\text{In}_{0.3}\text{Ga}_{0.7}\text{As}/\text{In}_{0.52}\text{Al}_{0.48}\text{As}$ strained layer QWIP using the light- and heavy-hole inverted intersubband transition. Figure 3.1.1 shows the strained QWIP energy band diagram. The p-type QWIP structure was grown on semi-insulating (SI) InP substrate along the [001] direction using MBE technique. Beryllium was used as the p-dopant and the structure consists of 20 periods of 4-nm $\text{In}_{0.3}\text{Ga}_{0.7}\text{As}$ quantum well (doped $1 \times 10^{18} \text{ cm}^{-3}$) separated by a 45-nm $\text{In}_{0.52}\text{Al}_{0.48}\text{As}$ undoped barrier. A 0.3 μm cap layer and a 1- μm bottom layer of $\text{In}_{0.53}\text{Ga}_{0.47}\text{As}$ were grown with a dopant density of $2 \times 10^{18} \text{ cm}^{-3}$ for ohmic contacts. The contact and barrier layers are lattice-matched with the SI InP substrate, and the well layer is in biaxial tension with a lattice mismatch of approximately 1.5% between the well and the barrier. In order to measure the spectral responsivity and dark current of the QWIP, a 200 by 200 μm^2 mesa structure was formed by using the chemical etching process.

Figure 3.1.2 shows the measured dark current characteristics and calculated differential resistance at $T = 77 \text{ K}$. It is noted that a very low dark current was obtained with nearly symmetry under the positive and negative biases in this p-type QWIP. The responsivity of the QWIP was measured as a function of temperature, bias voltage, and wavelength using a globar and an automatic PC-controlled single-grating monochromator system with a normal incidence IR illumination. The normalized responsivity versus wavelength for this QWIP is shown in Fig.3.1.3. Two peak wavelengths at $\lambda_{p1} = 7.8$ and $\lambda_{p2} = 10.8 \mu\text{m}$ were detected in the long-wavelength infrared (LWIR) detection band. The peak response at $\lambda_{p1} = 7.8 \mu\text{m}$ is resulted from the intersubband transition between the confined ground state (i.e., light-hole sub-band) to the continuum third heavy-hole band, while the peak response at λ_{p2} is attributed to the transition from the ground state to the continuum second heavy-hole band. The cutoff wavelength for $\lambda_{p1} = 7.8 \mu\text{m}$ was found to be 8.9 μm with a spectral bandwidth of $\Delta\lambda/\lambda_{p1} = 24\%$, while the cutoff wavelength for the $\lambda_{p2} = 10.8 \mu\text{m}$ was found to be 11.5 μm with a spectral bandwidth of $\Delta\lambda/\lambda_{p2} = 12\%$. The first heavy-hole sub-band is deeply confined in the well and the absorption peak is beyond 30 μm . Due to the thicker barrier layer, the photoresponse from this transition can not be detected.

The responsivity versus bias voltage for this p-QWIP is shown in Fig. 3.1.4. For $\lambda_{p2} = 10.8$

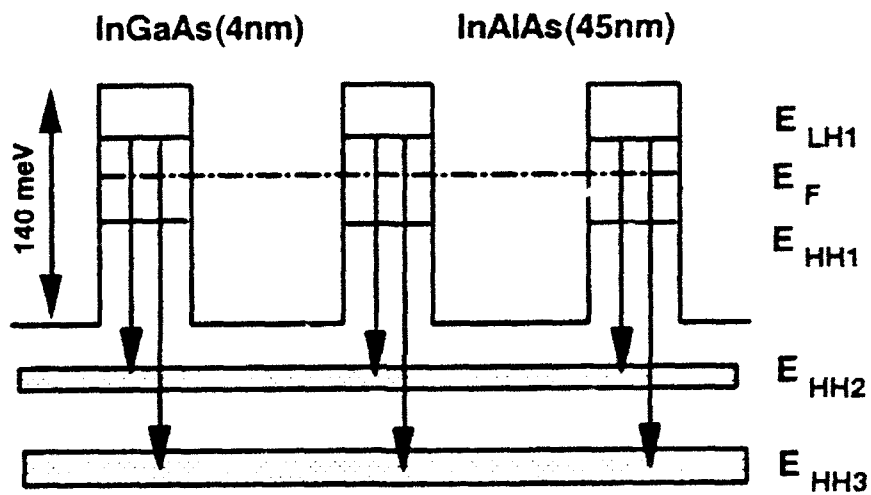


Figure 3.1.1 Energy band diagram of a p-type strained InGaAs/InAlAs QWIP showing the intersubband transitions from the inverted light hole states to the heavy hole continuum states.

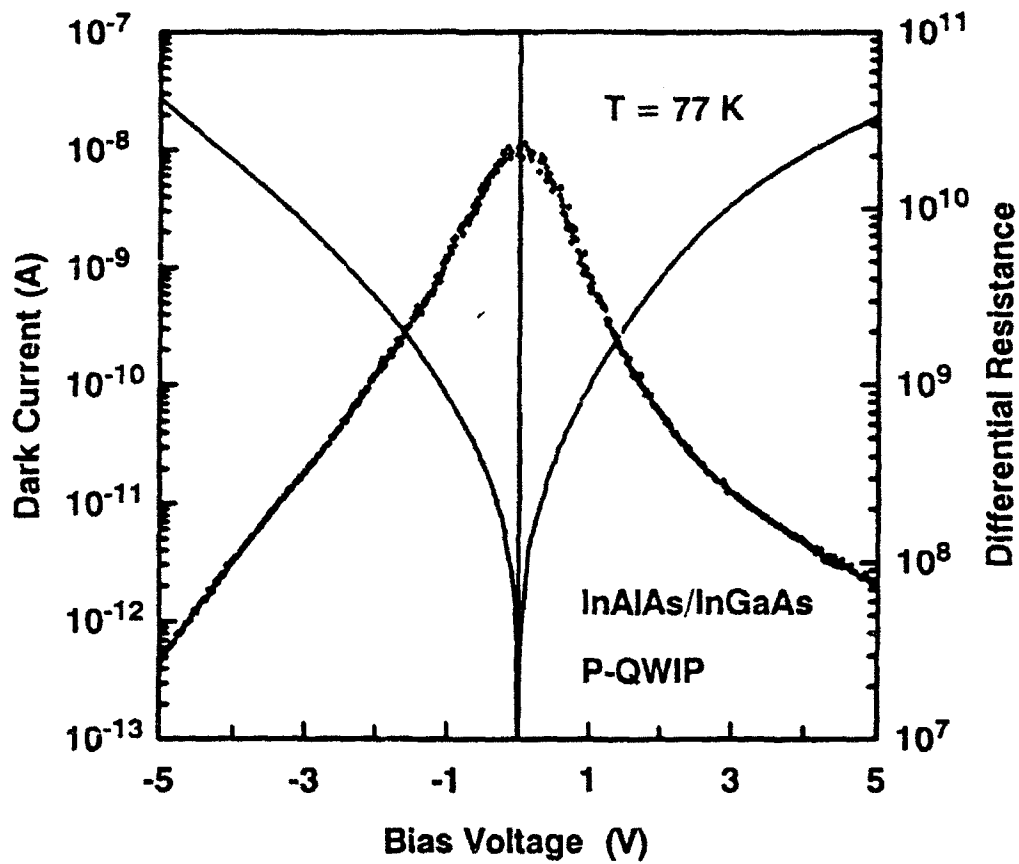


Figure 3.1.2 Dark current and differential resistance versus bias voltage of a p-type strained InGaAs/InAlAs QWIP at 77 K.

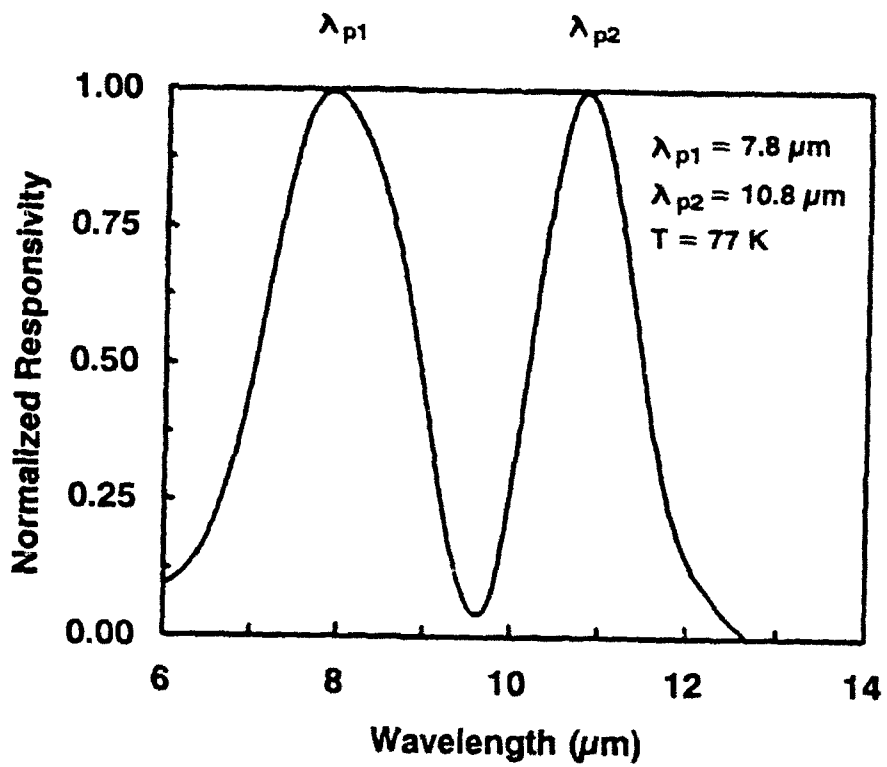


Figure 3.1.3 Normalized responsivity versus wavelength for a p-type strained InGaAs/InAlAs QWIP at 77 K.

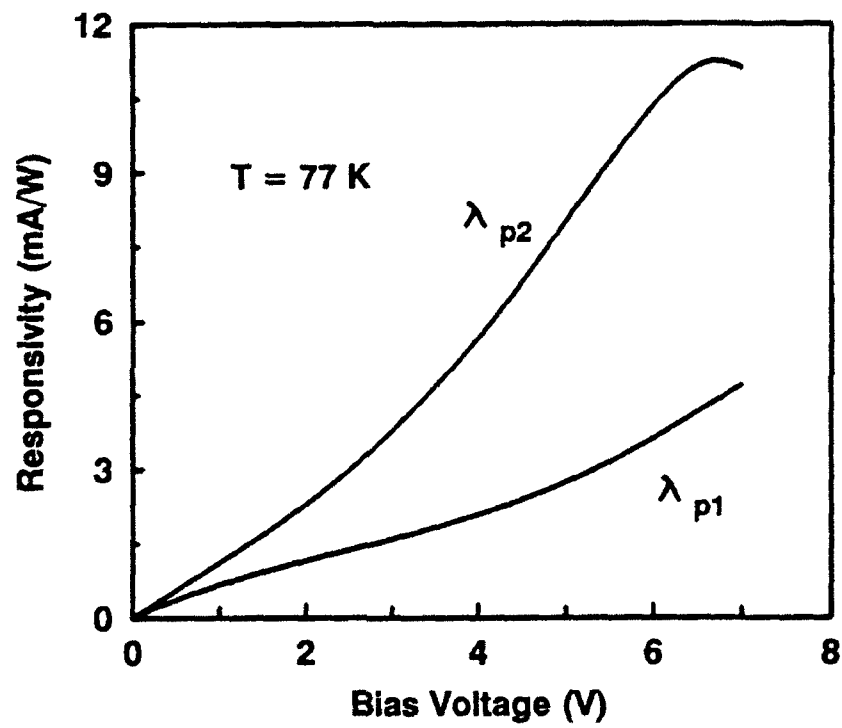


Figure 3.1.4 Responsivity versus bias voltage of a p-type strained InGaAs /InAlAs QWIP for $\lambda_{p1} = 7.8 \mu\text{m}$ and $\lambda_{p2} = 10.8 \mu\text{m}$, $T = 77 \text{ K}$.

μm , a maximum responsivity $R_A = 11 \text{ mA/W}$ was found at $V_b = 6 \text{ V}$ and $T = 77 \text{ K}$, which yielded a detectivity $D^* = 3.6 \times 10^9 \text{ cm-Hz}^{1/2}/\text{W}$. To our knowledge, this is the best detectivity value at $10.8 \mu\text{m}$ has ever been reported for a p-type QWIP. For $\lambda_{p1} = 7.8 \mu\text{m}$, the responsivity showed no saturation below $V_b = 8 \text{ V}$, and responsivity was found to be 3 mA/W at $v_b = 6 \text{ V}$ and $T = 77 \text{ K}$, and a detectivity $D^* = 1.5 \times 10^9 \text{ cm-Hz}^{1/2}/\text{W}$.

In conclusion, we have demonstrated a new two-color p-type strained layer InGaAs/InAlAs QWIP. The detectivity of the p-type QWIP was greatly enhanced due to the biaxial tensile strain introduced in the QWIP structure. The two-color spectral response in the LWIR band was the first ever achieved in a p-type QWIP. By optimizing the quantum well dopant density, strain strength, and structure parameters, a comparable performance to the n-type QWIPs could be obtained in the p-type strained layer InGaAs/InAlAs QWIPs.

3.2 The PV and PC Dual Mode Operation III-V QWIPs for Multicolor IR Detection

Summary: Four III-V quantum well infrared photodetectors (QWIPs) operating in the photoconductive (PC) and photovoltaic (PV) detection modes for the wavelength range from 2 to 14 μm are depicted. These dual-mode operation QWIPs were grown by the MBE technique using GaAs/AlGaAs and AlAs/AlGaAs and InGaAs/InAlAs material systems. Based on the bound-to-miniband (BTM) and enhanced bound-to-continuum (BTC) intersubband transition schemes, these detectors possess large absorption, low dark current, and high detectivity for the wavelengths of interest, and show promising for use in the large area IR focal plane array image sensor applications.

The III-V quantum well infrared photodetectors (QWIPs) based on intersubband transition schemes for detection in both the mid-wavelength infrared (3 - 5 μm) and long-wavelength infrared (8 - 14 μm) atmospheric spectral windows have been extensively investigated in recent years. A great deal of work has been reported on the lattice-matched GaAs/AlGaAs (GaAs-based) multiple quantum well and superlattice systems using bound-to-bound (BTB), bound-to-miniband (BTM), bound-to-quasi-continuum (BTQC) and bound-to-continuum (BTC) conduction intersubband transition mechanisms. Meanwhile, a variety of studies of the intersubband absorption has also been conducted in the lattice-matched InGaAs/InAlAs (InP-based) material system by using the BTB, and BTC intersubband transitions. Most of these QWIPs are operated in the photoconductive (PC) detection mode, while a few of them are operated in the photovoltaic (PV) detection mode. Due to the inherent low dark current, low Johnson noise current, and low power dissipation in the PV detection mode, it is highly desirable to develop high performance QWIPs using PV mode in

the temperature range of 65 to 85 K for infrared imaging sensor applications.

We report here four types of dual-mode (PC and PV) operation III-V QWIPs fabricated on lattice-matched GaAs/AlGaAs, AlAs/AlGaAs, and InGaAs/InAlAs material systems. These photodetectors (DM-QWIPs) are based on the bound-to-miniband (BTM), bound-to-continuum (BTC) conduction intersubband transition mechanisms. Figure 3.2.1 shows the energy band diagrams for these QWIPs (QWIP- A, B, C, and D). The photoresponse spectra of these QWIPs extend from the short-wavelength infrared (SWIR), mid-wavelength infrared (MWIR), to the long-wavelength infrared (LWIR) detection bands. The device parameters for these QWIPs are summarized in Table 3.2.1.

QWIP- A and C were grown on the semi-insulating (SI) (100) GaAs substrates by using molecular beam epitaxy (MBE) technique, while QWIP- D and B were grown on SI (110) GaAs substrate and SI(100) InP substrate, respectively. Each structure has a 1- μm -thick buffer layer (GaAs or $\text{In}_{.53}\text{Ga}_{.47}\text{As}$) with the n^+ doping density of $2 \times 10^{18} \text{ cm}^{-3}$, which was first grown on the SI substrate (GaAs or InP) for ohmic contact. The top ohmic contact of the QWIPs was formed on a 0.3 μm cap layer (GaAs or $\text{In}_{.53}\text{Ga}_{.47}\text{As}$) with a doping density of $2 \times 10^{18} \text{ cm}^{-3}$. For QWIP- B and C (i.e., BTM QWIPs), the barrier layer was formed by using a 6- period of undoped InGaAs/InAlAs or GaAs/AlGaAs superlattice barrier layers. The highly-doped enlarged quantum wells of QWIP- B and C are sandwiched between the undoped superlattice barrier layers. The QWIP- A structure consists of 40 periods of a very thick undoped barrier layer of $\text{Al}_{.25}\text{Ga}_{.75}\text{As}$ (875 Å) and a highly doped ($5 \times 10^{18} \text{ cm}^{-3}$) enlarged quantum well (110 Å). Due to heavy doping in the well both the ground state and first excited state in the well are populated by electrons at 77 K. As a result, each populated energy level in the well will make intersubband transition to the continuum states under IR photoexcitation. Due to a larger absorption strength from the excited state to continuum states as compared to the absorption strength from the ground state to the continuum states, a large enhanced absorption of the infrared radiation is expected in the excited state to the continuum states transition. Meanwhile the thicker barrier can greatly eliminate the undesirable tunneling current. The layer structure for QWIP- D is composed of AlAs/ $\text{Al}_{.5}\text{Ga}_{.5}\text{As}$ indirect bandgap materials, which is preferred to grow along the [110] direction of GaAs substrate. Since conduction band minima for the AlAs are located at the X-points (i.e. along [110] direction) of the Brillouin zone (BZ), the quantum well is formed by indirect bandgap AlAs while the indirect bandgap $\text{Al}_{.5}\text{Ga}_{.5}\text{As}$ becomes the barrier. As a result, a type-II energy band alignment is formed for this QWIP. Due to the anisotropic band structures and the tilted growth direction with respect

to principal axes of ellipsoidal valleys, it is possible to realize multi-band and multi-color normal incidence IR detection in a type-II AlAs/AlGaAs QWIP without using grating coupler.

The device structure for QWIP- A to D was formed by mesa-etching with an active area of $200 \times 200 \mu\text{m}^2$. To enhance absorption coupling efficiency in the quantum wells, planar one-dimensional (i.e. 1-D line: periodicity of $\Lambda = 5 \mu\text{m}$ with a geometrical ratio factor $g = d/\Lambda = 0.5$, d : metal strip width) or two-dimensional (i.e. 2-D double period: periodicity of $\Lambda = 10 \mu\text{m}$ with $g = d/\Lambda = 0.5$) metal grating couplers were formed on QWIP-A, B, and C by using E-beam evaporation of $0.2 \mu\text{m}$ Au film.

To analyze the intersubband transition schemes in these QWIPs, we performed theoretical calculations of the energy states E_{Wn} , E_{SLn} and E_{Cn} ($n = 1, 2, \dots$) in the well(W), superlattice (SL), and the continuum (C) state, and the transmission probability T^*T for the QWIPs using a multi-layer transfer matrix method (TMM). It is noted that a wide and highly degenerated global miniband is formed in the QWIP by using the superlattice barrier structure in the QWIP- B and C. In the type-II QWIP- D, there are two bound states, $E_{W1,2}$, in the AlAs X-band well and four continuum states, E_{C2-5} , in the X-band, which can find their resonant pair levels in the Γ -band, while the continuum state E_{C1} is located below the Γ -band minima of the $\text{Al}_{1.5}\text{Ga}_{3.5}\text{As}$ layers (see Fig.3.2.1 (D)).

Measurements of the dark currents for all the QWIP samples were performed in the temperature range from 30 K to 85 K using a HP-4145 Parameter Analyzer. Figure 3.2.2 shows the current-voltage (I-V) curves for these QWIPs. The asymmetrical I-V characteristics with I_d being larger for positive bias than negative bias were observed in these QWIPs. In the BTM QWIPs (B and C), the asymmetry is mainly ascribed to two effects: (1) superlattice-formed miniband asymmetrical conduction which was observed in the optical processes in thin multilayer semiconductor structures, (2) dopant migration from the doped quantum well to the undoped barrier region, which is further modified the asymmetrical conduction miniband. In the BTC QWIPs (A and D), the asymmetrical I-V characteristics are mainly due to the energy band bending effect (resulting from dopant migration) and heavy doping effect.

The responsivities of the QWIPs were measured as a function of temperature, bias voltage V_b , polarization direction, and wavelength using a globar and automatic PC controlled single-grating monochromator spectral measurement system with a normal incidence IR illumination. The normalized responsivity versus wavelength for the QWIPs (A - D) are shown in Fig.3.2.3.

The absolute peak responsivities R_A (or R_V) for the QWIPs were measured and calibrated using a room temperature pyroelectric detector. Table 3.2.2 summarizes the measured and calculated peak wavelengths, cutoff wavelengths, responsivities, and detectivities for the four QWIPs studied in this work.

In QWIP-A, two response peaks were detected: one at $\lambda_p = 7.7 \mu\text{m}$ with PV mode operation and the other at $\lambda_p = 12 \mu\text{m}$ with PC mode detection ($V_b > 1 \text{ V}$). In the PV mode, a peak voltage photoresponsivity, $R_V = 11,000 \text{ V/W}$, at $\lambda_p = 7.7 \mu\text{m}$ with a spectral bandwidth of $\Delta\lambda/\lambda_p = 18 \%$ was obtained, which is attributed to the transition from the ground state E_{W1} to the first continuum states E_{C1} above the barrier. This internal photovoltage results from the spatial charge separation when the asymmetrical energy band bending occurs due to dopant migration and heavy doping effect. When a bias voltage is applied to the detector, the PV response at $\lambda_p = 7.7 \mu\text{m}$ disappears, and the PC mode conduction becomes the dominant detection mechanism. In the PC detection mode, the peak wavelength shifts from $7.7 \mu\text{m}$ to $12 \mu\text{m}$. A maximum responsivity, R_A , of 0.48 A/W was measured for this QWIP at $V_b = 2 \text{ V}$. The cutoff wavelength for this QWIP was found to be $\lambda_c = 13.2 \mu\text{m}$ with a spectral bandwidth $\Delta\lambda/\lambda = 18.3 \%$.

For QWIP-B, it has a peak wavelength at $\lambda_p = 10 \mu\text{m}$ in the PV mode detection, and a peak wavelength at $\lambda_p = 10.3 \mu\text{m}$ in the PC mode at $T = 67 \text{ K}$. The intersubband transitions for both PC and PV modes is attributed to the resonant transition from the ground state E_{W1} to the global miniband states E_{SL1} which are aligned with the first excited state E_{W2} in the quantum well. The resonant transition (i.e. maximum absorption strength) depends strongly on the location of the first excited state E_{W2} relative to the miniband E_{SL1} ⁵. In QWIP-B, the E_{W2} lies near the top of the miniband E_{SL1} which will result in a strong, narrow-band spectral response of $\Delta\lambda/\lambda_p = 7 \%$ and $0.3 \mu\text{m}$ short wavelength shift in the PV detection mode. Note that the BTM QWIP operating in the PV mode offers a unique feature of ultra-narrow bandwidth infrared detection, which is not attainable in a conventional QWIP structure. As the bias voltage increases (in the PC mode), relative position between the "embedding" localized state E_{W2} and the "framing" miniband state E_{SL1} can be adjusted by a "controlling bias" due to the different dependence of E_{W2} and E_{SL1} on the bias voltage. At $V_b = 0.5 \text{ V}$ and $T = 67 \text{ K}$, a broad-band spectral linewidth of $\Delta\lambda/\lambda_p = 24 \%$ was obtained which is about factor 3 increasing spectral bandwidth compared to the PV mode operation. QWIP-C sample has the same BTM intersubband transition mechanism as QWIP B, which also shows a similar characteristics for both the PV and PC mode detection. In QWIP-C, a peak wavelength at $\lambda_p = 8.9 \mu\text{m}$ with cutoff wavelength of $\lambda_c = 9.3 \mu\text{m}$ was observed for both PV

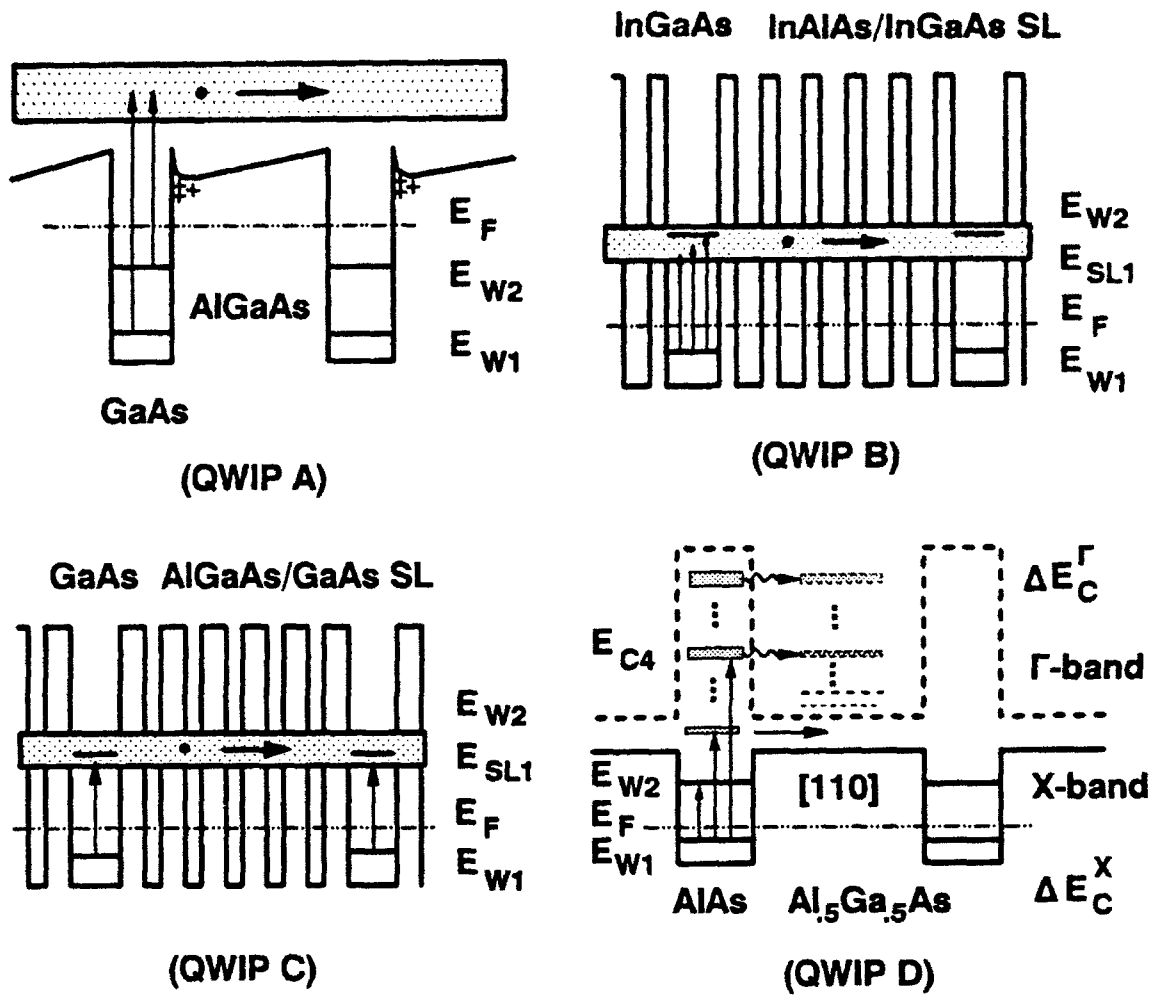


Figure 3.2.1 Energy band diagrams for four type-I and type-II III-V QWIPs using the BTM and BTC intersubband transition schemes.

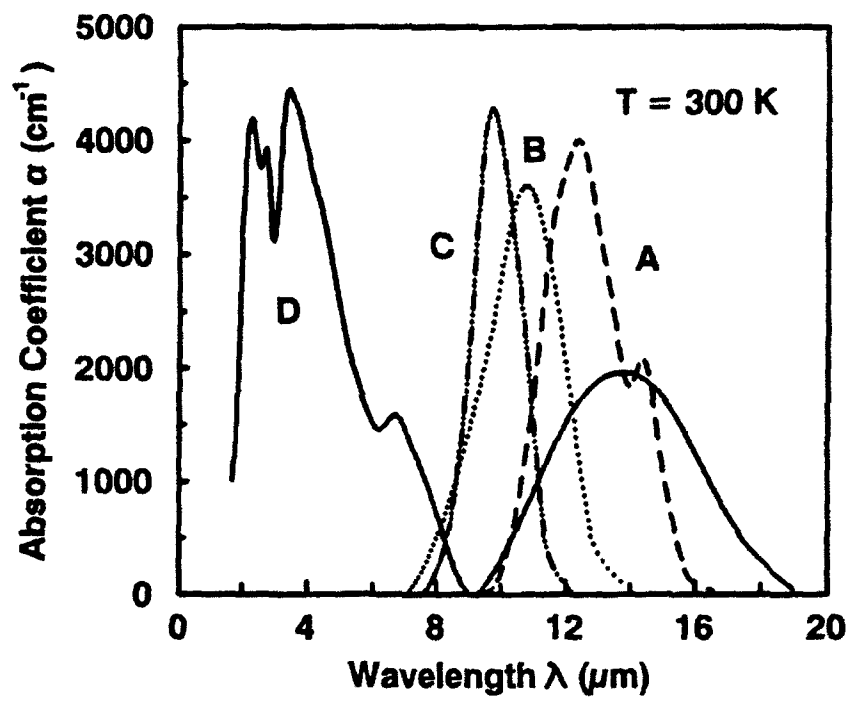


Figure 3.2.2 Optical absorption for the four III-V QWIPs showing in Fig.3.2.1.

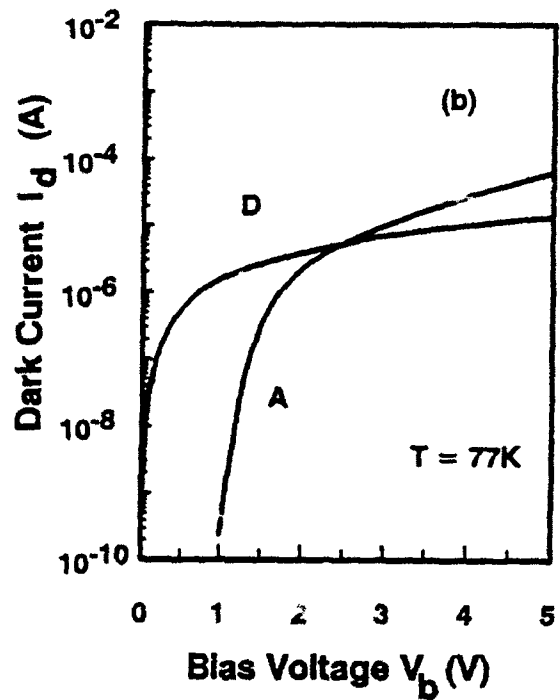
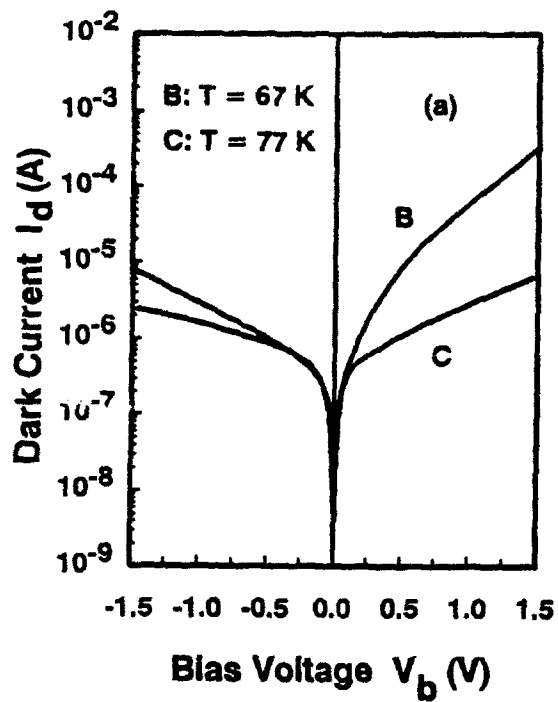


Figure 3.2.3 Dark current versus bias voltage the four III-V QWIPs showing in Fig.3.2.1.

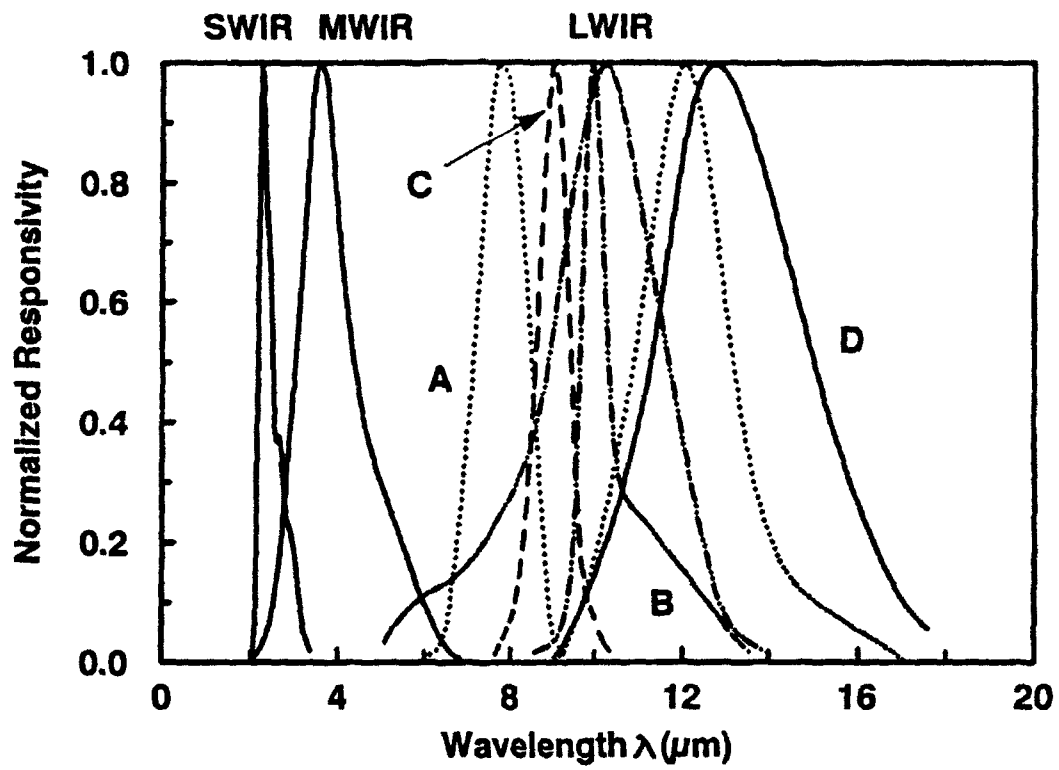


Figure 3.2.4 Normalized responsivity versus wavelength for the four III-V QWIPs showing in Fig.3.2.1.

Table 3.1 Device parameters for the four types of III-V QWIPs shown in Fig.3.2.1.

QWIP (Type)	L_W (\AA)	L_B (\AA)	N_D $10^{18} \text{ (cm}^{-3}\text{)}$	QW periods	Grating coupler	Intersubband transition
A (I)	GaAs 110	$\text{Al}_{.25}\text{Ga}_{.75}\text{As}$ 875	5	40	1-D $5 \mu\text{m}$	BTC
B (I)	$\text{In}_{.53}\text{Ga}_{.47}\text{As}$ 110	InGaAs/InAlAs 46/30	0.5	20	2-D $10 \mu\text{m}$	BTM
C (I)	GaAs 88	GaAs/AlGaAs 29/58	2	40	1-D $10 \mu\text{m}$	BTM
D (II)	AlAs 30	$\text{Al}_{.5}\text{Ga}_{.5}\text{As}$ 500	2	20		BTC

Table 3.2 Summary of the peak and cutoff wavelengths, responsivity, and detectivity for the four types of QWIPs shown in Fig.3.2.1.

QWIP	λ_p (μm)	R (A/W)	λ_c (μm)	D^* $\text{cm}\cdot\text{Hz}^{1/2}/\text{W}$
A	12 (PC)	0.48	13.2	1.0×10^{10}
	7.7 (PV)	11,000 (V/W)	8.5	1.5×10^9
B	10.3 (PC)	0.038	11.7	5.8×10^9
	10 (PV)	12,000 (V/W)	10.4	5.7×10^9
C	8.9 (PC)	0.23	9.3	1.2×10^{10}
	8.9 (PV)	0.15	9.2	7.5×10^9
D	2.2 (PC)	110	2.45	1.1×10^{12}
	2.2 (PV)	64,000 (V/W)	2.45	1.4×10^{10}
	3.5 (PC)	18.3	4.3	3.0×10^{11}
	3.5 (PV)	58,000 (V/W)	4.3	1.2×10^{10}
	12.5 (PC)	0.024	14.8	1.1×10^9

and PC modes, which is attributed to the transition from the ground state E_{W1} to the miniband states E_{SL1} . In contrast to QWIP- B, the resonant state E_{W2} of QWIP- C lies near the bottom of the miniband states, E_{SL1} , which gives rise to a narrow bandwidth absorption peak of the $\Delta\lambda/\lambda_p = 8.5\%$ for the PV mode, and yields a resonant peak wavelength coincidence at $\lambda_p = 8.9\ \mu\text{m}$ for both the PV and PC modes.

QWIP- A to C discussed above offer a dual-mode detection in the LWIR (8 - 14 μm) band, which can be realized by using either the BTM conduction scheme or by adjusting the QWIP structure parameters. However, due to the energy band offset limitation and a very fine geometrical grating coupler requirement, the dual-mode operation in the MWIR and SWIR detection bands using the intersubband transition schemes discussed above becomes very difficult. Some researchers reported the PV mode detection in the MWIR band using an ultra-thin ballistic transport and resonant barrier or Γ -band and X-band coupling technique with the help of grating coupling method. In QWIP-D, we used an AlAs/AlGaAs type-II QWIP structure in the intersubband transition scheme with a direct normal incidence without using a grating coupler. In this QWIP, the two main peak wavelengths were detected at $\lambda_p = 2.2$ and $3.5\ \mu\text{m}$ which fall in the SWIR and MWIR bands. The SWIR band has two peak wavelengths at $\lambda_p = 2.2\ \mu\text{m}$ and $\lambda \sim 2.7\ \mu\text{m}$, while the MWIR spectral band has a peak wavelength at $\lambda_p = 3.5\ \mu\text{m}$ and a long tail attributed to a contribution at about $\lambda \sim 4.8\ \mu\text{m}$. The positions for all four peak wavelengths observed are in excellent agreement with the values deduced from the FTIR measurements and theoretical calculations. In addition to the SWIR and MWIR band responses, a broad LWIR absorption band (i.e., 9 to 18 μm) was also observed in the PC mode operation of this QWIP with a peak response wavelength at $\lambda_p = 12.5\ \mu\text{m}$.

In conclusion, we have demonstrated four new dual-mode detection QWIPs using the BTM and BTC intersubband transition schemes and operating between $T = 65\ \text{K}$ and $85\ \text{K}$. In the LWIR detection band, both QWIP-A and C offer good detectivities ($D^* = 10^9$ and $1.2 \times 10^{10}\ \text{cm}\sqrt{\text{Hz}}/\text{W}$) for the PV and PC detection modes. By properly optimizing the QWIP structures, the performance of the BTM QWIPs in PV mode operation can be further improved. The dual-mode detection in the SWIR and MWIR bands was also observed in the AlAs/AlGaAs type-II QWIP. This QWIP shows a great potential for multi-color and multi-band infrared image sensor applications.

3.3. A normal incidence type-II QWIP using an indirect $AlAs/AlGaAs$ grown on (110) GaAs for the mid- and long-wavelength multi-color detection

Summary: A normal incidence type-II indirect $AlAs/Al_{0.5}Ga_{0.5}As$ QWIP grown on (110) GaAs by MBE technique for the mid- and long- wavelength multicolor IR detection has been developed. The normal incident excitation of long wavelength intersubband transition was achieved in the [110] X-band confined AlAs quantum wells. Six absorption peaks including four from X-band to Γ -band intersubband resonant transitions were observed at wavelengths, $\lambda_{p1-6} = 2.2, 2.7, 3.5, 4.8, 6.5$ and $12.5 \mu m$. The resonant transport from X-band to Γ -band gives rise to high photoconductive gain, which is highly desirable for focal plane arrays (FPAs) image sensor applications.

The intersubband absorption and infrared detection using type-I and type-II quantum well infrared photodetectors (QWIPs) have been investigated extensively in recent years¹⁻⁹. In type-I quantum well structure, the direct bandgap material system is used and hence the shape of constant energy surfaces is usually spherical. As a result, only the component of IR radiation with electric field perpendicular to the quantum well layers will give rise to intersubband transition in the quantum well. Therefore, no intersubband absorption in the quantum wells is expected for normal incidence illumination in type-I quantum well QWIPs. In order to achieve strong absorption of normal incidence IR radiation in the quantum wells, grating coupled structures or indirect bandgap semiconductors are highly desirable for QWIP applications. In the indirect bandgap materials, conduction electrons occupy indirect valleys with ellipsoidal constant energy surfaces. The effective-mass anisotropy (mass tensor) of electrons in the ellipsoidal valleys can provide coupling between the parallel and perpendicular motion of the electrons when the principal axes of one of the ellipsoids are tilted with respect to the growth direction. As a result of the coupling, intersubband transitions at normal incidence in an indirect bandgap QWIP structure are allowed.

Since the $AlAs/Al_{0.5}Ga_{0.5}As$ system is an indirect bandgap material, the conduction-band minima for the AlAs quantum wells are located at the X- point of the Brillouin zone (BZ). The constant energy surface will also undergo change from a typical sphere at the zone center for a direct bandgap material (i.e. GaAs) to off-center ellipsoids of an indirect bandgap material (i.e. AlAs). For AlAs, there are six ellipsoids along [100] axes with the centers of the ellipsoids located at about three-fourth of the distance from the BZ center. By choosing a proper growth direction such as [110], [111], [113], [115] directions, due to the anisotropic band structures and the tilted growth direction with respect to principal axes of ellipsoidal valley, it is possible to realize large

area normal incidence IR detection in AlAs/AIGaAs QWIPs.

Recently we reported a normal incidence type-II QWIP using an indirect AlAs/AlGaAs system grown on (110) GaAs substrate. We use the indirect bandgap AlAs for the quantum well layer and $Al_{0.5}Ga_{0.5}As$ for the barrier layer. Since $Al_xGa_{1-x}As$ becomes an indirect bandgap material for $x > 0.45$, the conduction-band minimum shifts from the Γ -band to the X-band. Analyzing band ordering in the AlAs/ $Al_{0.5}Ga_{0.5}As$ MQW is a complicated subject in photonic device engineering. We have used large enough quantum well and barrier layer thicknesses (> 10 monolayers) so that the QWIP under study has a type-II band structure. The conduction band offset of $Al_{0.5}Ga_{0.5}As$ relative to AlAs is about 170 meV. Figure 3.3.1 (a) shows a schematic conduction-band (Γ - and X-bands) diagram for the type-II indirect AlAs/ $Al_{0.5}Ga_{0.5}As$ quantum well structure, in which electrons are confined inside the AlAs QW layer. The intersubband transition energy levels between the ground bound state (E_0) in the AlAs quantum well and the first excited state (E_1) in the well or the continuum states ($E_2 \dots E_6$) above the $Al_{0.5}Ga_{0.5}As$ barrier layers are also shown in Fig.3.3.1(a). It is noted that band splitting between the Γ -band and the X-band edge is about 50 meV in the AlGaAs layer, and the conduction band offset in the Γ -band is found to be 630 meV. The constant energy surfaces near the X-conduction valleys of AlAs grown on (110) GaAs is shown in Fig.3.3.1 (b).

The indirect bandgap AlAs/AIGaAs QWIP structure was grown on a (110) GaAs substrate by using the molecular beam epitaxy (MBE) technique. A $1.0 \mu\text{m}$ thick n -GaAs buffer layer with $N_d = 2 \times 10^{18} \text{ cm}^{-3}$ was first grown on the [110] oriented semi-insulating GaAs substrate, followed by the growth of 20 periods of AlAs/ $Al_xGa_{1-x}As$ quantum wells with a well width of 30 Å and doping concentration of $2 \times 10^{18} \text{ cm}^{-3}$. The barrier layers on either side of the quantum well consist of an undoped $Al_{0.5}Ga_{0.5}As$ (500 Å) barrier layer. Finally, a $0.3 \mu\text{m}$ thick n^+ -GaAs cap layer with a dopant density of $2 \times 10^{18} \text{ cm}^{-3}$ was grown on top of the quantum well layers for ohmic contacts. The doping concentration of $2 \times 10^{18} \text{ cm}^{-3}$ in the quantum well is chosen so that only the ground state is populated, and tradeoff between the low dark current and strong absorption strength are considered.

To derive the basic equations for the normal induced intersubband transitions and the corresponding indirect type-II QWIPs, we start with the Hamiltonian description of quantum mechanics for an electron, which is given by

$$H_0 = \frac{p^2}{2m} + V(\mathbf{r}) + \frac{\hbar}{4m^2c^2} \boldsymbol{\sigma} \cdot (\nabla V(\mathbf{r}) \times \mathbf{p}), \quad (1)$$

where m , p , and σ are the mass, momentum, and spin operators on an electron, respectively. $V(\mathbf{r})$ is a periodic potential function. The system under consideration consists of an assembly of electrons and the infrared radiation field. The Hamiltonian of this system, H , may be written as the sum of the unperturbed Hamiltonian H_0 and the perturbing Hamiltonian H'_{rad} which represents the interaction between the electrons and the incident infrared photon written as

$$H'_{rad} = -\frac{q}{mc} \mathbf{A} \cdot [\mathbf{P} + (\frac{\hbar}{4mc^2}) \sigma \times \nabla V], \quad (2)$$

where \mathbf{A} is the vector potential of the IR radiation field and \mathbf{P} is the canonical momentum.

The matrix element of intersubband transition in the quantum well is given by^{13,14}

$$M_{fi} = \int \phi_{kf} H'_{rad} \phi_{ki} d\mathbf{r} = -q \left(\frac{2\pi}{Vcn\hbar\omega} \right)^{1/2} \mathbf{e}_\omega \cdot \nabla_{\mathbf{k}} \mathcal{E}_{\mathbf{k}} \quad (3)$$

where $\phi_{ki(or f)}$ is the total wavefunction for a state in i th (or f th) intersubband, the parameters i and f denote the initial and final states, \mathbf{e}_ω is the unit polarization vector of the incident photon, ω is the light frequency, q is the electronic charge, V is the volume of the crystal, n is the refractive index at the wavelength of incident IR radiation, and $\mathcal{E}_{\mathbf{k}}$ is the conduction band energy of the X-valley material in the well.

It can be shown that the intersubband transition probability $\eta_{\mathbf{k}}$ may be expressed as

$$\begin{aligned} \eta_{\mathbf{k}} &= \frac{2\pi}{\hbar} |M_{fi}|^2 \delta(E_f - E_i - \hbar\omega) \\ &= \frac{B_0 k_z^2}{\omega} \left[\frac{\partial^2 \mathcal{E}_{\mathbf{k}}}{\partial k_x \partial k_x} (\mathbf{e}_\omega \cdot \mathbf{x}_0) + \frac{\partial^2 \mathcal{E}_{\mathbf{k}}}{\partial k_x \partial k_y} (\mathbf{e}_\omega \cdot \mathbf{y}_0) + \frac{\partial^2 \mathcal{E}_{\mathbf{k}}}{\partial k_x \partial k_z} (\mathbf{e}_\omega \cdot \mathbf{z}_0) \right]^2 \delta(E_f - E_i - \hbar\omega) \quad (4) \end{aligned}$$

where B_0 is a constant equal to $\frac{q^2 \pi^2}{cVn\hbar^2}$; \mathbf{x}_0 , \mathbf{y}_0 , and \mathbf{z}_0 are the directional unit vectors. The result indicates that the nonzero intersubband transition probability at normal incidence can be obtained only when either of the crossover terms in the second partial derivatives is nonzero.

For an indirect gap type-II AlAs quantum well layer grown along [110] direction of GaAs substrate, due to the tilted anisotropic energy band with minimum point away from BZ center (see Fig.1b), the second partial derivatives $\frac{\partial^2 \mathcal{E}_{\mathbf{k}}}{\partial k_i \partial k_i}$ ($i = x, y$) can be different from zero. Therefore, it is possible to excite long wavelength intersubband transitions in the quantum well under normal incidence IR radiation. However, for a direct type-I system (i.e. GaAs) due to the isotropic spherical energy surface and the axis symmetrical parabolic band $E = E_z + \hbar^2(k_y^2 + k_z^2)/2m^*$, it always has $\frac{\partial^2 \mathcal{E}_{\mathbf{k}}}{\partial k_x \partial k_x} = 0$, (where $i \neq z$). The corresponding transition probability becomes

$$\eta_{\mathbf{k}} = \frac{B_0 k_z^2}{\omega} \left[\frac{\partial^2 \mathcal{E}_{\mathbf{k}}}{\partial k_x \partial k_x} (\mathbf{e}_\omega \cdot \mathbf{z}_0) \right]^2 \delta(E_f - E_i - \hbar\omega) \quad (5)$$

Equation (5) reveals that optical transitions would become zero for type-I structures under normal incidence radiation.

To analyze the intersubband transition mechanism and energy level positions in a type-II AlAs/AlGaAs QWIP, theoretical calculations of the energy states E_n , ($n = 0, 1, 2, \dots$) for the X-band and Γ -band and the transmission coefficient $T * T$ for the QWIP were performed by using a multi-layer transfer matrix method¹⁶. To determine the intersubband transition levels, we use the one-band effective mass approximation (see Appendix) and take into account the effects of band nonparabolicity and electron-electron interaction. In comparison with the more sophisticated energy band models such as two-band and three-band models, the one-band effective mass approach will give the first order approximation, thus yielding a reasonable prediction for the QWIP performance. The simulated results are summarized in Table 3.3.1. The each energy levels shown in the Table 3.3.1 are referred to the center of its band width. It is noted that E_0 (ground state) and E_1 (first excited state) are bound states which are confined in the AlAs X-band well, while E_2 to E_6 are all continuum states. The continuum states in the X-band can find their resonant pair levels in the Γ -band except E_2 which is located below the Γ -band minima (about 30 meV).

A BOMEM interferometer was used to measure the infrared absorbance of the AlAs/AlGaAs QWIP sample. In order to eliminate substrate absorption, we performed absorbance measurements with and without the quantum well layers. The absorbance data were taken using normal incidence at 77 K and room temperature. The absorption coefficients deduced from the absorbance data are shown in Fig. 3.3.2. Two absorption peaks at wavelengths $\lambda = 6.8 \mu\text{m}$ and $14 \mu\text{m}$ were detected, while four additional absorption peaks at $\lambda = 2.3 \mu\text{m}$, $2.7 \mu\text{m}$, $3.5 \mu\text{m}$, and $4.8 \mu\text{m}$ at NIR were also observed. The measured absorption peak wavelengths are in excellent agreement with the theoretical prediction. All the absorption coefficients measured at 77 K were found to be about a factor of 1.2 higher than the room temperature values. From our theoretical analysis, the $14 \mu\text{m}$ peak with an absorption coefficient of about 2000 cm^{-1} is attributed to the transition between the ground state E_0 and the first excited state E_1 in quantum well, while the $6.8 \mu\text{m}$ peak with absorption coefficient of about 1600 cm^{-1} is due to transition between the ground state E_0 and the continuum state E_2 . The absorption peaks at $2.3 \mu\text{m}$, $2.7 \mu\text{m}$, $3.5 \mu\text{m}$, and $4.8 \mu\text{m}$ are attributed to the transitions between the ground state E_0 and other high order continuum states listed in Table I. It is interesting to note that the high order intersubband transitions have relatively larger absorption coefficient of about 4000 cm^{-1} , which is quit different from the intersubband transition in type-I QWIPs. However, the absorption at $6.8 \mu\text{m}$, which is also due to the transition between bound

state and continuum state, has a small absorption coefficient compared to the other high order continuum transitions. This indicates that the 6.8 μm absorption peak has a different absorption and conduction mechanism, which we shall discuss it later.

To facilitate the normal incidence IR illumination, an array of $210 \times 210 \mu\text{m}^2$ mesas were chemically etched down to n^+ -GaAs buffer contact layer on the GaAs substrate. Finally, AuGe/Ni/Au ohmic contact was formed on top of the QWIP structures, leaving a central sensing area of $190 \times 190 \mu\text{m}^2$ for normal incidence illumination. Device characterization was performed in a liquid-helium cryogenic dewar. A HP4145 semiconductor parameter analyzer was used to measure the dark current versus bias voltage. Figure 3.3.3 shows the measured dark current as a function of the bias voltage for temperatures between 68 and 89 K. Substantial reduction of device dark current was achieved in the present type-II structure. The photocurrent was measured using a CVI Laser Digikrom 240 monochromator and an ORIEL ceramic element infrared source. A pyroelectric detector was used to calibrate the radiation intensity from the source. The measured data for the QWIP are tabulated in Table 3.3.2, which showed six absorption peaks. The peaks for $\lambda_{p1,2}$ only exhibited the photoconductive (PC) detection mode, while the peaks for λ_{p3-6} operated in both the PC mode and photovoltaic (PV) mode.

Figure 3.3.4 shows the detector's photoresponse and absorption coefficient for wavelengths from 9 to 18 μm . The peak photoresponse was observed at $\lambda_{p1} = 12.5 \mu\text{m}$ with a cutoff wavelength at 14.5 μm and a peak responsivity of $R_A = 24 \text{ mA/W}$ at $T = 77\text{K}$ and $V_b = 2 \text{ V}$. A broader spectral bandwidth of $\Delta\lambda/\lambda = 30\%$ was obtained for this QWIP, which is larger than the type-I QWIP¹⁷. The property of a broader spectral bandwidth within X-band intersubband transition was also found in [113] GaAs substrate growth direction⁸. Detectivity for this peak wavelength was found to be about $1.1 \times 10^9 \text{ cm (Hz)}^{1/2}/\text{W}$ under the above specified condition. A relative small absorption peak at $\lambda_{p2} = 6.5 \mu\text{m}$ was detected, which is attributed to the transition between the ground state E_0 and the first continuum state E_2 . The peak responsivity for λ_{p2} was found to be about $R_A = 5 \text{ mA/W}$ at $T = 77 \text{ K}$ and $V_b = 2 \text{ V}$, which was not shown in the figure. About 8 ~ 11 meV blueshifts were found in these peak wavelengths.

Figure 3.3.5 shows the normalized photovoltaic (PV) spectral response bands at the peak wavelengths of $\lambda_{p4} = 3.5 \mu\text{m}$ and $\lambda_{p6} = 2.2 \mu\text{m}$. The two spectral response bands cover wavelengths from 2.2 μm to 6.5 μm for $\lambda_{p4} = 3.5 \mu\text{m}$ and from 2.0 μm to 3.25 μm for $\lambda_{p6} = 2.2 \mu\text{m}$. The spectral band for λ_{p6} has an additional peak at $\lambda_{p5} \sim 2.7 \mu\text{m}$, while the spectral band for λ_{p4} also has a

large tail which results from another peak contribution at about $\lambda_{p3} \sim 4.8 \mu\text{m}$. The positions for all four peak wavelengths λ_{p3-6} are in excellent agreement with the values deduced from the FTIR measurements and theoretical calculations. The main peak responses occurred at $\lambda_{p4} = 3.5 \mu\text{m}$ and $\lambda_{p6} = 2.2 \mu\text{m}$ with responsivities of $R_A = 29 \text{ mA/W}$ and 32 mA/W , respectively, at $T = 77 \text{ K}$. The responsivities of two main peaks have a different voltage dependence. The peak for λ_{p4} increases rapidly for $V_b > 0.5 \text{ V}$, and it reaches a saturation responsivity value of 18.3 A/W at $V_b \geq 3 \text{ V}$ as shown in Fig. 3.3.6. On the other hand, the responsivity for λ_{p6} remains nearly constant for $V_b \leq 2 \text{ V}$, and then exponentially increases to $R = 110 \text{ A/W}$ at $V_b \sim 6 \text{ V}$, as shown in Fig. 3.3.7. Extremely large photoconductivity gains of 630 and 3,200 for λ_{p4} and λ_{p6} (as compared to the value at $V_b = 0$) were obtained at $V_b = 3 \text{ V}$ and 6 V , respectively. In a type-II indirect AlAs/AlGaAs QWIP, free carriers are confined in the AlAs quantum well formed in the X-conduction band minimum, which has a larger electron effective mass than that in the Γ -band valley. When a normal incidence radiation impinges on this QWIP, electrons in the ground-state of the X-well are excited to either the excited state E_1 or one of the continuum states E_2 to E_6 . If the continuum state in the X-band valley is resonantly aligned with a state in the Γ -band valley, the photon-generated electrons in the X-band will undergo resonant transport to the resonant state in the Γ -band provided that the barrier layer (in the present case, AlAs layer) is so thin that it is transparent to the conduction electrons^{18,19}. This resonant transport from X-band to Γ -band is expected to be a coherent resonance which can greatly enhance the transmission if the electron lifetime τ_L^Γ in these continuum states is much shorter than the X-band to Γ -band scattering time constant τ_S . The τ_L^Γ can be estimated from the uncertainty principle, $\tau_L^\Gamma = \frac{\hbar}{\Delta E_{FWHM}} \sim 10 \text{ fs}$ (where ΔE_{FWHM} is the spectral full width at half maximum), while $\tau_S \sim 1 \text{ ps}$ ²⁰, hence $\tau_L^\Gamma \ll \tau_S$. The peak transmission at resonance is expected to be increased by the ratio of $\tau_S/\tau_L^\Gamma \sim 100$. In addition, due to the effective mass difference between the X-band and the Γ -band, electron velocity and mobility in the Γ -valley will be much higher than the value in the X-band valley. Since the photocurrent is proportional to the electron velocity and mobility (i.e., $I_{ph} = Aqv_d g \tau_R$, where A is the effective area of the detector, v_d is the drift velocity, g is the photogeneration rate, $1/\tau_R$ is the recombination rate of electrons in the Γ -band), a large increase in the photocurrent is expected when photon-generated electron resonant transition from the X-band to Γ -band takes place under certain bias conditions. It is known that optical gain $G = \tau_L/\tau_T$, where τ_T is transit time ($\tau_T = \frac{l}{\mu F}$, l is the superlattice thickness, μ is the electron mobility, and F is the electric field). In the coherent resonance and certain bias condition, G will be significantly enlarged as well. The larger responses at λ_{p4} and λ_{p6} wavelengths are due to a better alignment of these

resonant levels, while the relatively lower responses for the λ_{p3} and λ_{p5} wavelengths are ascribed to a slightly misalignment in the resonant levels, which results from the X- Γ coupling strength difference²¹. However, no photoconductivity gain is expected not to be observed at λ_{p1} and λ_{p2} peak wavelengths due to the absence of the resonant transition from the X-band to the Γ -band in the electronic conduction. Due to the novel resonant conduction scheme from the X-band to the Γ -band, a long wavelength IR QWIP with extremely high responsivity and ultra low noise can be fabricated from the type-II indirect AlAs/AlGaAs material system grown on (110) GaAs described in this paper.

The PV mode operation at peak wavelengths of λ_{p3-6} in the type-II AlAs/AlGaAs QWIP is resulted from the macroscopic polarization field (i.e. Hartree potential) caused by the energy band bending effect and spatial separation of electrons and holes. However, the PV operation was not observed in the wavelengths of λ_{p1-2} . This is probably due to the novel resonant transport feature which enhances the photogenerated electron conduction.

In conclusion, we have demonstrated a normal incidence type-II QWIP using an indirect X-band AlAs/Al_{0.5}Ga_{0.5}As system grown on (110) GaAs substrate with multispectral responses in the 2 to 14 μm wavelength range. The desirable normal incidence radiation is allowed due to the tilted and anisotropic energy band structure of AlAs/ AlGaAs grown on a (110) GaAs substrate. The detector was found to have six peak wavelength responses at $\lambda_{p1-6} \approx 2.2, 2.7, 3.5, 4.8, 6.5,$ and $12.5 \mu\text{m}$. The spectral responses for wavelengths at $\lambda_p = 2.2, 2.7, 3.5,$ and $4.8 \mu\text{m}$ are ascribed to the novel resonant interaction between the X-band and Γ -band which yields a large photoconductive gain in electron conduction. The spectral response at $\lambda = 12.5 \mu\text{m}$ has a broader bandwidth ($\Delta\lambda/\lambda = 30\%$), covering the wavelength range from 9 to 18 μm . The capabilities of normal incidence, large spectral sensing range, ultra high photoconductive gain, multispectral detection, and ultra-low noise characteristics make this type-II AlAs/AlGaAs QWIP highly desirable for many infrared applications. Further studies of the interaction effects between the X- and Γ -bands, transition coupling, bandgap engineering, and hot electron transport mechanisms in the type II indirect III-V multiple quantum well structures may lead to the development of a variety of novel quantum well infrared detectors, lasers, and modulators.

Appendix

By using the transfer matrix method, a energy dispersion equations for periodic structures such as multiple quantum wells and superlattices can be deduced. It is assumed that each layer contains sufficient number of atomic sublayers (i.e. monolayers) so that the effective-mass model holds for the calculation. From the effective-mass model, the solution of the conduction band envelope function for j th region can be obtained from

$$\phi_j'' + k_j^2 \phi_j = 0,$$

where k is the wave propagation constant $k = \sqrt{\frac{2m^*(E-V_p)}{\hbar^2}}$, V_p conduction-band offset energy, and E electron energy. When k is either real or imaginary, the equation gives either oscillatory or evanescent wave solution, respectively. For a flat-band condition, the functions of ϕ and ϕ_j'/m_j^* should be continuous cross the heterointerfaces. The wave conduction property for the system (i.e. multiple quantum wells or superlattice) can be represented by the characteristic impedance $Z^s = m^*/k$ which is associated with the ratio of $\phi/(\phi'/m^*)$. The transfer matrix T of the one periodic superlattice structure which itself consists of N layers is given by

$$T = \begin{pmatrix} T_{11} & T_{12} \\ T_{21} & T_{22} \end{pmatrix} = \prod_{j=1}^N \begin{pmatrix} \cos k_j L_j & Z_j^s \sin k_j L_j \\ -\frac{1}{Z_j^s} \sin k_j L_j & \cos k_j L_j \end{pmatrix},$$

where L_j is the thickness of a layer in the superlattice. The dispersion equation for the system is readily found to be given by $T_{11} + T_{22} = 2 \cos qL$, where q is the superlattice wave vector, L the period of the superlattice ($=\sum_{j=1}^N L_j$). The conduction band nonparabolicity, bias-dependent property, and coupling between X-band and Γ -band could be also included in the transfer matrix expression to give a complicated energy dispersion relation.

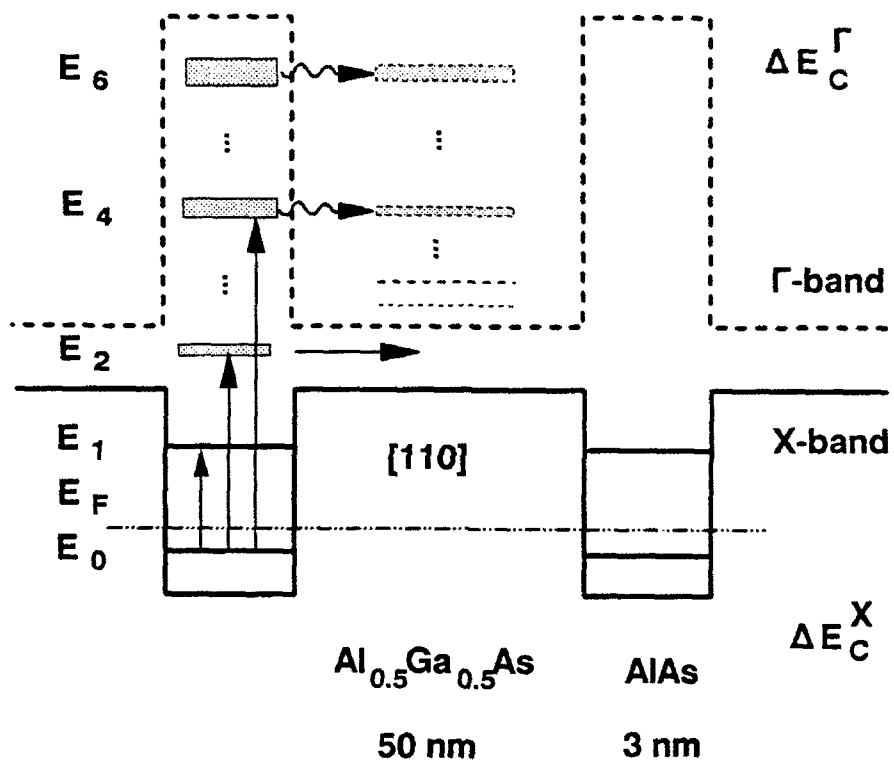


Figure 3.3.1 (a) Energy band diagram of a type-II AlAs/AlGaAs QWIP, showing the energy levels (E_0 E_6) in the X- and Γ -conduction valleys, and the intersubband transitions.

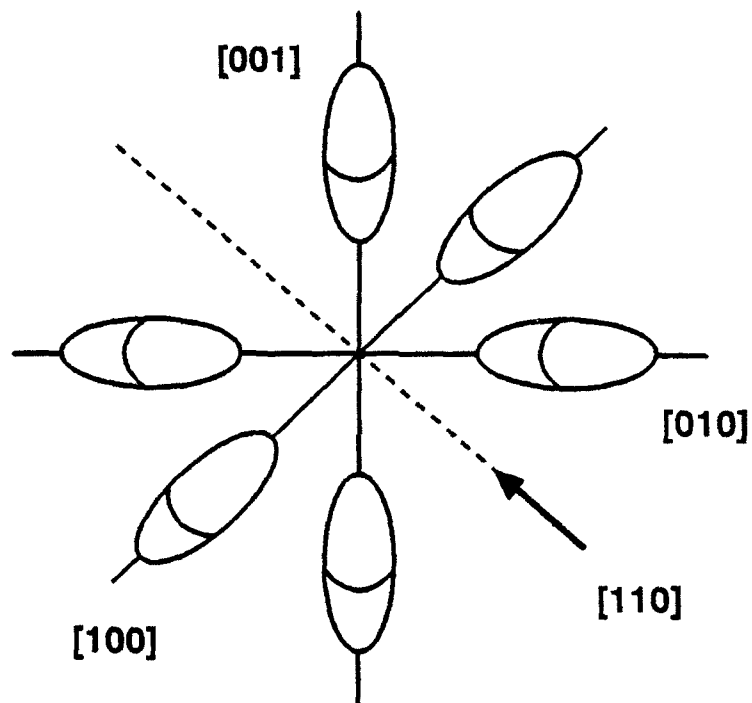


Figure 3.3.1 (b) Constant energy surfaces near the X-conduction valleys of AlAs grown on [110] GaAs substrate.

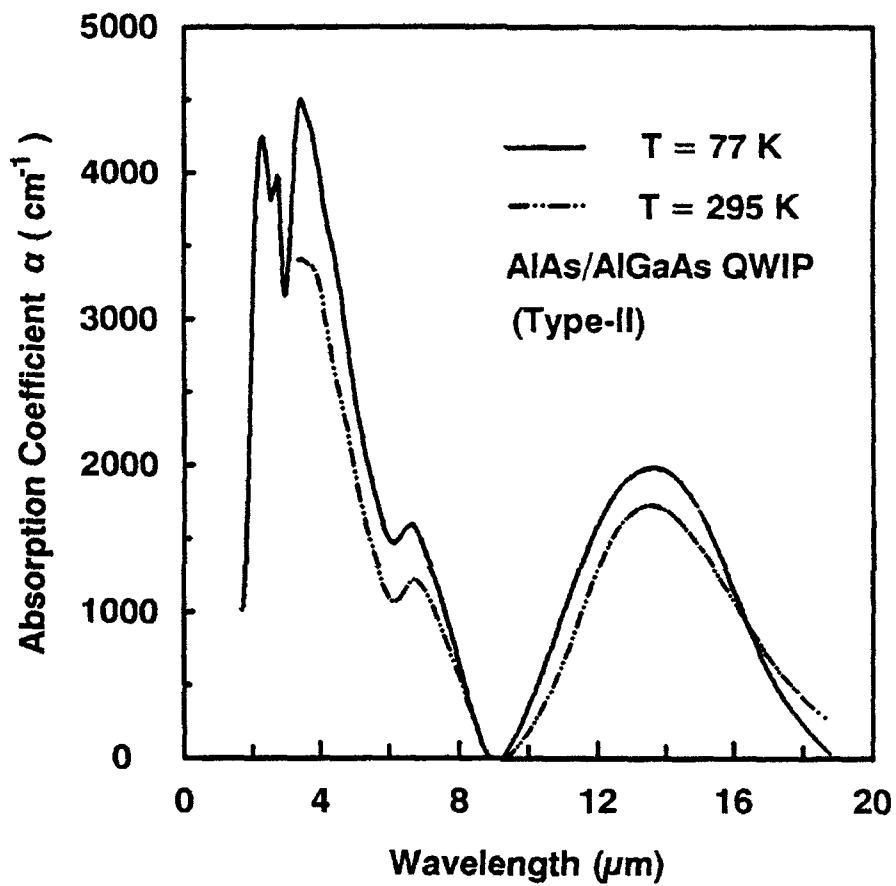


Figure 3.3.2 Optical absorption coefficients deduced from absorbance data for AlAs/AlGaAs QWIP measured at 77 K and 295 K.

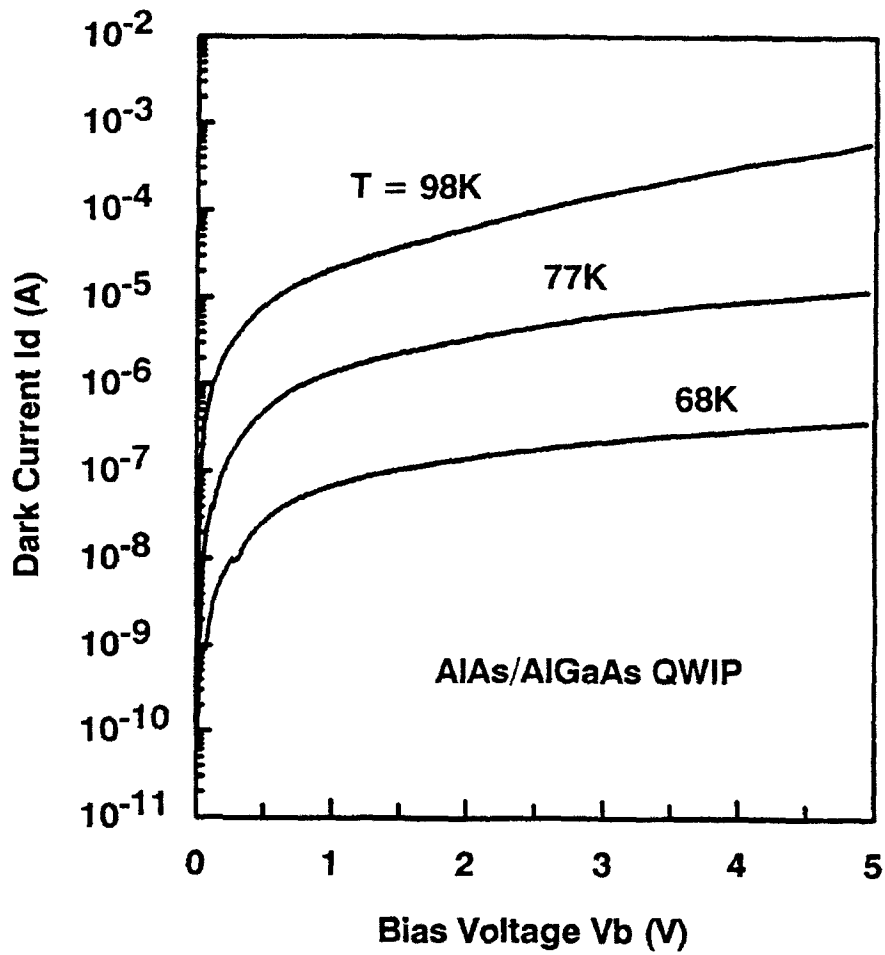


Figure 3.3.3 Dark current versus bias voltage for the AlAs/AlGaAs QWIP measured at 98, 77 and 68 K.

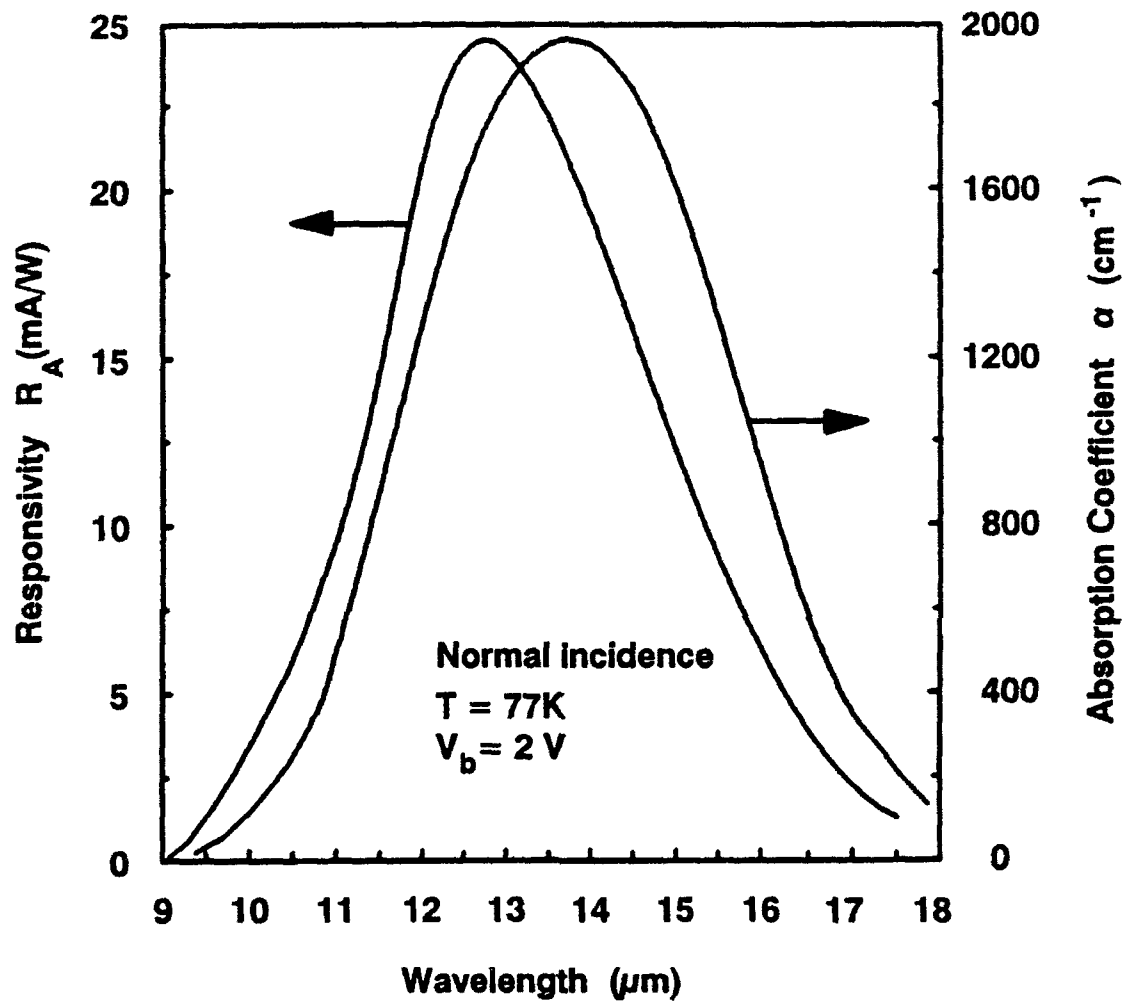


Figure 3.3.4 Responsivity and optical absorption coefficient vs. wavelength for the AlAs/AlGaAs QWIP measured at 77 K and $V_b = 2\text{V}$.

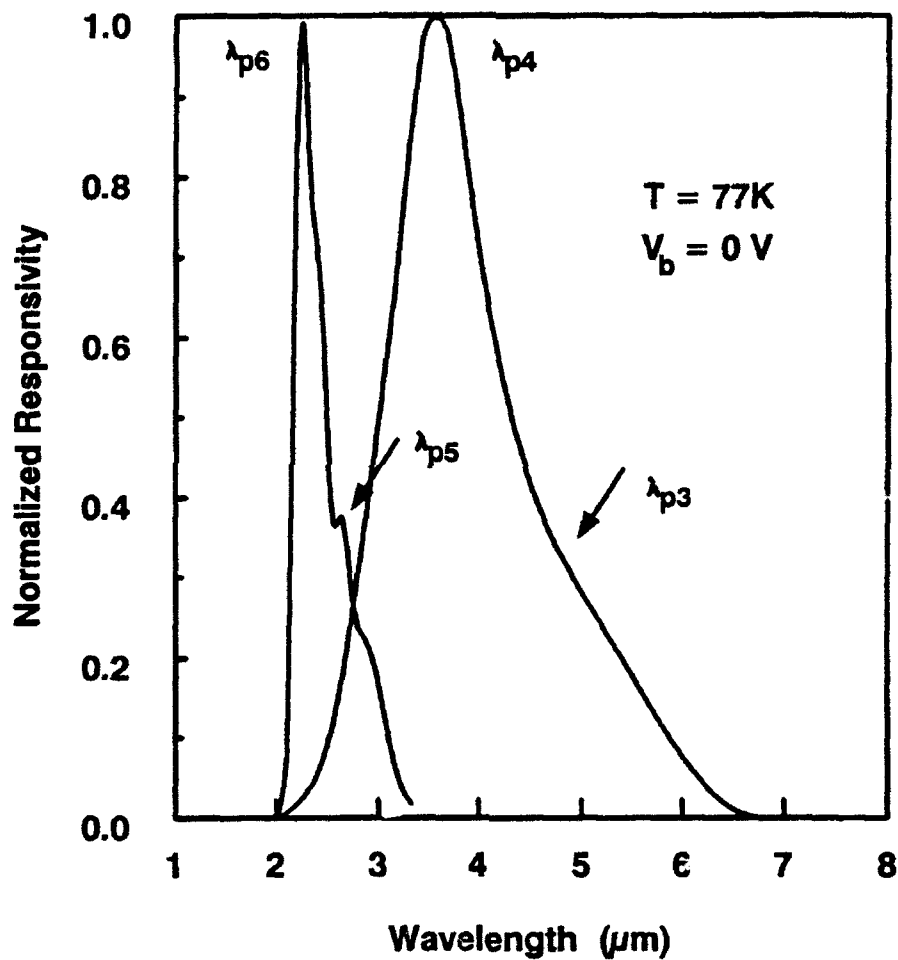


Figure 3.3.5 Normalized responsivity versus wavelength for the AlAs/AlGaAs QWIP measured at 77 K and $V_b = 0$ V, showing four peak responses corresponding to the intersubband transitions from E_1 to E_3 , E_4 , E_5 , and E_6 .

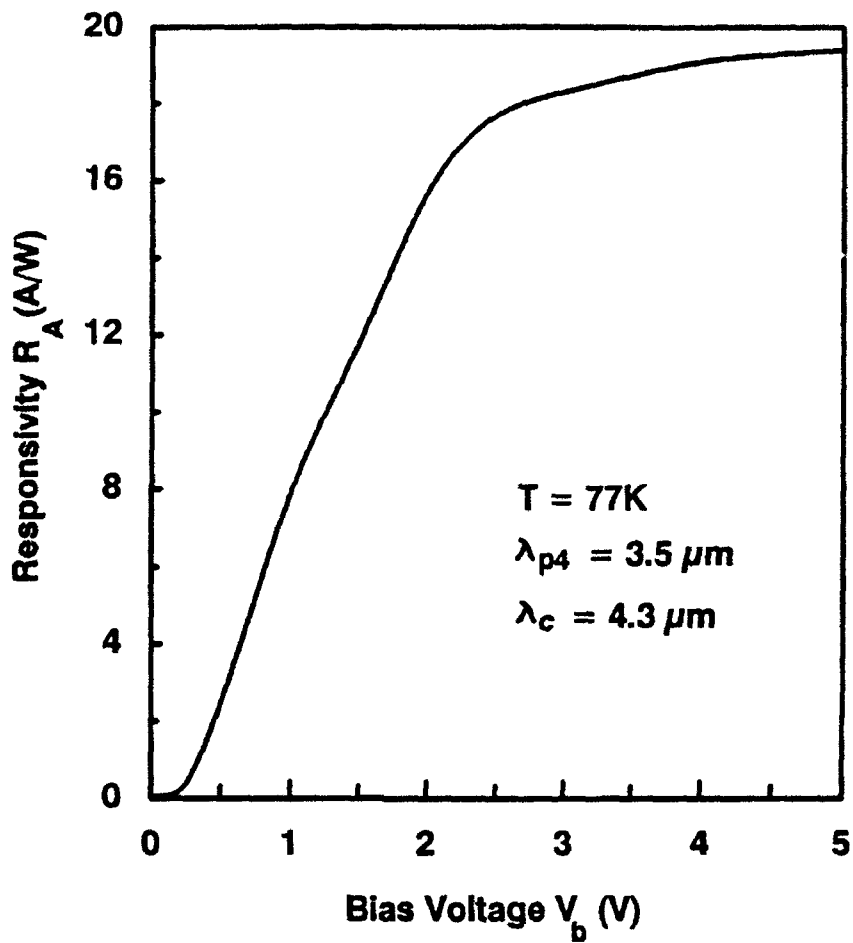


Figure 3.3.6 Responsivity versus bias voltage for the AlAs/AlGaAs QWIP measured at 77 K and $\lambda_{p4} = 3.5 \mu\text{m}$.

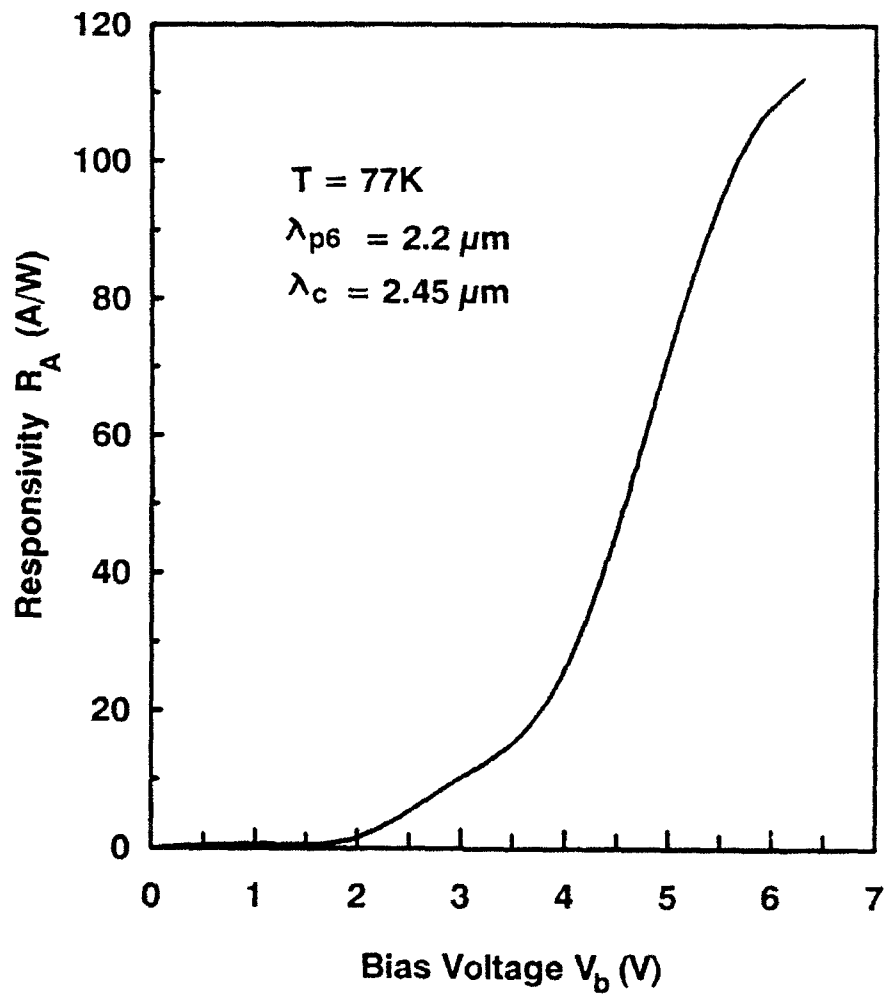


Figure 3.3.7 Responsivity versus bias voltage for the AlAs/AlGaAs QWIP measured at 77 K and $\lambda_{p6} = 2.2 \mu m$.

	E_0	E_1	E_2	E_3	E_4	E_5	E_6
X-band	20	110	189	270	365	475	600
Γ -band				265	370	460	595

Table 3.3.1 The simulated intersubband transition energy levels in the X-band and Γ -band for the type-II AlAs/AlGaAs QWIP. The energy levels, E_3 , E_4 , E_5 , and E_6 in the Γ -band and X-band formed the resonant levels for the photoexcited electrons in this QWIP. The parameters used in the calculation of X-band and Γ -band are $m^* = 0.78 m_0$, $0.15 m_0$ for AlAs and $0.82 m_0$, $0.11 m_0$ for $\text{Al}_{0.5}\text{Ga}_{0.5}\text{As}$. (Note: All the energy levels shown are measured from the AlAs quantum well X- conduction band edge in unit of meV.)

	λ_{p1}	λ_{p2}	λ_{p3}	λ_{p4}	λ_{p5}	λ_{p6}
Peak (μm)	12.5	6.5	4.8	3.5	2.7	2.2
R_A (A/W) (PV)				0.029		0.032
R_A (A/W) (PC)	0.024	0.005		18.3		110
	2 V	2 V		3 V		6 V
D^* ($\text{cm}\sqrt{\text{Hz}}/\text{W}$)	1.1×10^9			3.0×10^{11}		1.1×10^{12}

Table 3.3.2 The measured peak wavelengths, responsivities, and detectivities for the type-II AlAs/AlGaAs QWIP at $T = 77$ K.

3.4 A 2-D Square Mesh Metal Grating Coupled InGaAs/InAlAs BTM QWIP

Summary A theoretical and experimental study of the coupling quantum efficiency and responsivity in an InGaAs/InAlAs BTM QWIP by using a planar 2-D square mesh metal grating has been carried out. A coupling quantum efficiency of $\eta = 29\%$ was obtained using a grating period, $g = 4 \mu\text{m}$ and grating width, $a = 2.5 \mu\text{m}$ at peak response wavelength $\lambda_p = 10 \mu\text{m}$.

In this section we describe a 2-D double periodic square mesh metal grating coupler for coupling the IR radiation in a BTM QWIP under normal incident backside illumination. The 2-D square mesh metal grating offers several advantages which include: (i) Efficiently scattering the normal incident IR radiation into the quantum wells with an absorbable angle independent of light polarization, and (ii) easy to fabricate such a planar metal grating structure on the QWIP surface, as shown in Fig.3.4.1. In the design of a 2-D square mesh metal grating coupler, the aperture width 'a' and the grating period 'g' are the two key parameters which govern the coupling quantum efficiency of the QWIPs. It can be shown that the power of the higher order diffracted waves for such a grating structure is a function of the ratio 'a/g', which is called the 'strip factor'. For effective coupling, values of the strip factor ($= a/g$) for a square mesh metal grating coupler must fall between 0.55 and 0.63.

A theoretical and experimental study of the coupling quantum efficiency and responsivity in an $\text{In}_{0.48}\text{Al}_{0.52}\text{As}/\text{In}_{0.53}\text{Ga}_{0.47}\text{As}$ bound-to-miniband (BTM) QWIP enhanced by using a 2-D square mesh metal grating coupler with grating width $a = 2.5 \mu\text{m}$ and grating period $g = 4 \mu\text{m}$ under backside normal incidence illumination has been carried out. The QWIP sample was grown by the molecular beam epitaxy (MBE) technique. A $1\text{-}\mu\text{m}$ -thick highly doped ($2 \times 10^{18} \text{ cm}^{-3}$) n^+ - $\text{In}_{0.53}\text{Ga}_{0.47}\text{As}$ bottom contact layer was first grown on a lattice matched semi-insulating InP substrate. This is followed by the growth of 20 periods of enlarged $\text{In}_{0.53}\text{Ga}_{0.47}\text{As}$ quantum wells with a well width of 110 \AA and a dopant density of $5 \times 10^{17} \text{ cm}^{-3}$. The barrier layers on each side of the quantum well consist of 6 periods of undoped $\text{In}_{0.52}\text{Al}_{0.48}\text{As}(35 \text{ \AA})/\text{In}_{0.53}\text{Ga}_{0.47}\text{As}(50 \text{ \AA})$ superlattice layers. A second highly-doped ($2 \times 10^{18} \text{ cm}^{-3}$) n^+ - $\text{In}_{0.53}\text{Ga}_{0.47}\text{As}$ cap layer of $0.3 \mu\text{m}$ thick was grown to complete the structure and served as the top ohmic contact for the QWIP. The square mesas of $200 \times 200 \mu\text{m}^2$ area were formed by chemical etching the active layers down to the bottom contact layer. A square contact ring using AuGe/Ni/Au film was first deposited around the periphery of the mesa structure and then alloyed for ohmic contact formation. The metal grating was then formed on the QWIP by using electron beam (e-beam) evaporation of Au film directly

onto the mesa surface followed by lift-off process.

Figure 3.4.1 shows the square mesh metal grating structure formed on the top face of an InGaAs QWIP, where $a = 2.5\mu\text{m}$ is the aperture width and $g = 4\mu\text{m}$ is the grating period. The square apertures are arranged in the conducting screen along two orthogonal coordinates \hat{x} and \hat{y} making the whole grating structure as equal spaced parallel metal lines intersect one another. The unknown electromagnetic waves near the grating can be modeled by using modal expansion method. Taking wave theory in a periodic structure into consideration, the transverse vector fields of incident, reflected and transmitted waves are expressed as sums of Floquet modes $\vec{\Phi}_{pqr}$, where (p, q) is the diffracted order, $r = 1$ denotes the TE Floquet modes, $r = 2$ denotes the TM Floquet modes. Using the method of moments, the matrix form is obtained as

$$[Y_m^M] [W_m] = [I_m] \quad (6)$$

where

$$Y_m^M = \sum_{pq} \sum_{r=1}^2 (\xi_{pqr} + \xi_{pqr}^d) C_{pqr}^{M*} C_{pqr}^m$$

$$C_{pqr}^m = \int \int_{-a/2 \leq x, y/2} \vec{\Phi}_{pqr}^* \cdot \vec{\Psi}_m dx dy \quad (7)$$

and incident dependent matrix,

$$I_m = 2 \cdot \sum_{r=1}^2 A_{00r} \xi_{00r}^d C_{00r}^{m*} \quad (8)$$

The $\vec{\Psi}_m$ are the waveguide modes spanned by the aperture, W_m represents the corresponding expansion coefficient, ξ_{pqr} and ξ_{pqr}^d are the admittance of the Floquet modes at two sides of the mesh grating, and A_{00r} are the coefficients of the incident fields. The integrals C_{pqr}^m are complex numbers, so are the elements of Y_m^M . The absorption constant α of a QWIP depends on $\cos^2 \gamma^9$, where γ is the angle between the electric field vector of the diffracted mode and the free carrier motion vector \hat{z} in the quantum wells. It is noted that only the TM propagating Floquet modes of the grating scattered field will produce intersubband absorption and photo-response. Besides, a larger $\cos^2 \gamma$ implies a larger absorption constant, where the cosine of angle γ is given by

$$\cos \gamma_{pq2} = \frac{\lambda/n_r}{g} \cdot \sqrt{p^2 + q^2} \quad (9)$$

where n_r is the refractive index of the medium in which the wave propagates. It is worthy of noting that the coupling quantum efficiency of a grating coupled QWIP depends not only on γ but also on the power of each higher order TM propagating modes, which can be expressed as

$$\eta = \sum_i P_i \cdot (1 - e^{-\alpha_i d}) \quad (10)$$

where \mathcal{P}_i is the normalized power of each effective (propagating) i th order TM mode, α_i is the corresponding absorption constant, and l is the total length of the doped quantum wells. In the present case, $l = (110\text{\AA}) \times (20 \text{ periods}) = 2200\text{\AA}$. Figure 3.4.2 shows the relative power and angle of the first and second orders of the diffracted waves for square mesh grating coupled InGaAs BTM QWIP. The second order diffracted waves become dominant for λ shorter than $10.465\mu\text{m}$. By substituting the values of $\cos \gamma$ and \mathcal{P}_i given in Fig.3.4.2 and Eq.(5), a coupling quantum efficiency of 32% was obtained at $\lambda = 10\mu\text{m}$ for the square mesh metal grating coupled InGaAs BTM QWIP under backside illumination. It is worthy of noting that the coupling quantum efficiency can be further improved by choosing a smaller grating period. According to our numerical analysis, the optimum grating coupler has the normalized parameters $\frac{\lambda_p/n_r}{g} \approx 1$, and $a/g = 0.6$, where λ_p is the wavelength corresponding to peak absorption. Therefore, a grating with $g = 3\mu\text{m}$ and $a = 1.8\mu\text{m}$ should yield a maximum coupling quantum efficiency for this InGaAs QWIP.

The photocurrent measurements were carried out using a global IR source, an ORIEL 77250 single grating monochromator, a current preamplifier and a chopper lock-in amplifier system. The sample was mounted in a closed-cycle liquid helium cryogenic system. The incident IR radiation intensity was measured by using a calibrated pyro-detector. Figure 3.4.3 shows a comparison of the measured and calculated responsivity versus wavelength for the square mesh metal grating coupled InGaAs BTM QWIP with grating period $g = 4\mu\text{m}$ and grating width $a = 2.5\mu\text{m}$. Note that the responsivity of the QWIP was calculated by substituting the coupling quantum efficiency given in Eq. (5) into the following expression

$$R_p = \eta \cdot g_o \cdot \frac{\lambda}{1.24} \quad (11)$$

where the optical gain $g_o = 0.09$ was obtained from the noise gain measured at 77 K using the assumptions that these two gains are equal and remain invariant from 77 K to 61 K. The measured coupling quantum efficiency $\eta = 29\%$ at peak response $\lambda_p = 10\mu\text{m}$ is slightly smaller than that of the calculated value. This may be attributed to the fact that the conductivity of metal grating (Au) in a real QWIP device is smaller than the theoretical value of infinity. The current loss in the conducting mesh metal grating will certainly lower the value of coupling quantum efficiency measured in a practical QWIP device.

In conclusion, we have performed a theoretical and experimental study of the coupling quantum efficiency and responsivity in a 2-D square mesh metal grating coupled InGaAs BTM QWIP under normal incident backside illumination. The measured coupling quantum efficiency for an InGaAs BTM QWIP was found to be 29% with grating parameters $g = 4\mu\text{m}$ and $a = 2.5\mu\text{m}$. The coupling

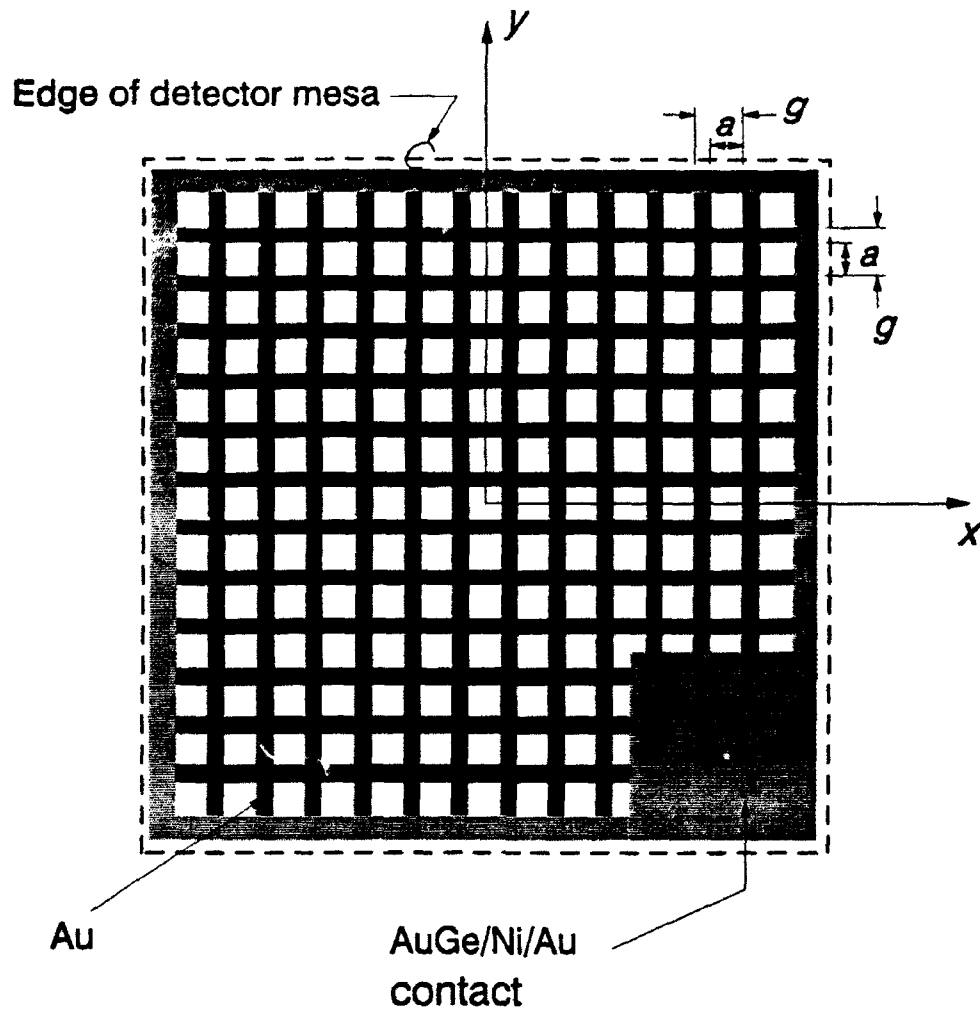


Figure 3.4.1 Top view of a 2-D square mesh metal grating coupler formed on an InGaAs BTM QWIP.

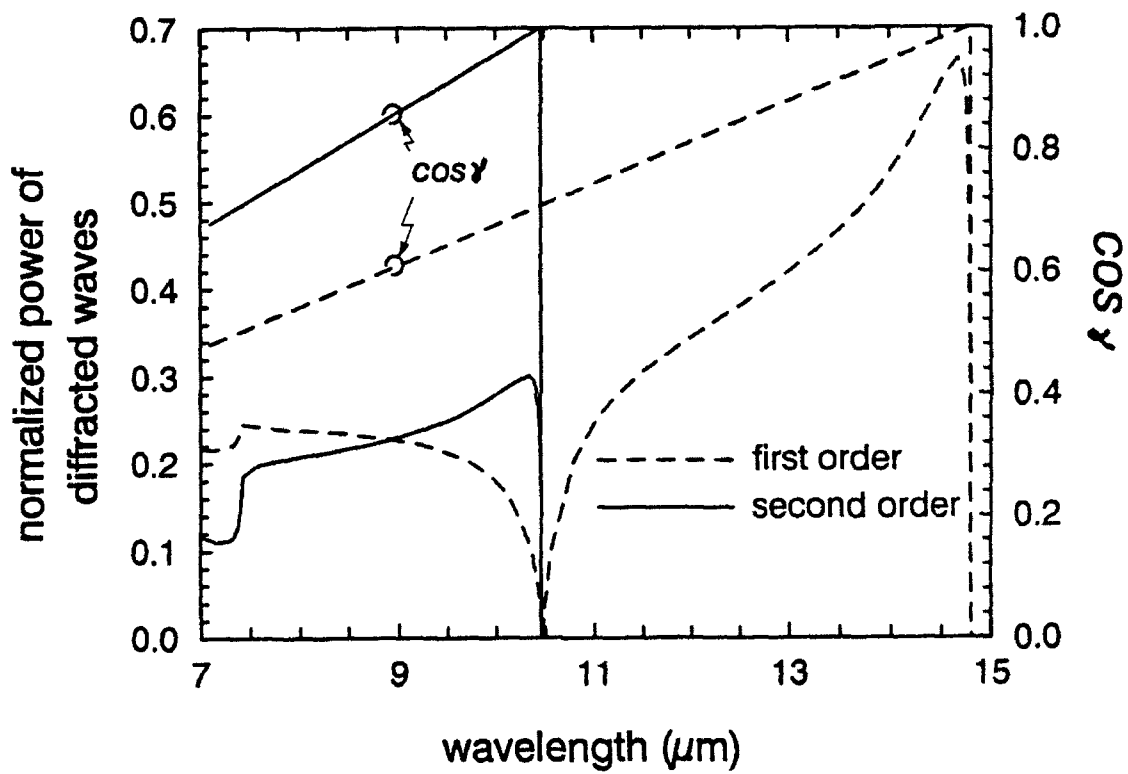


Figure 3.4.2 Normalized power of the 1st. and 2nd order diffracted waves for a 2-D square mesh metal grating coupled InGaAs BTM QWIP.

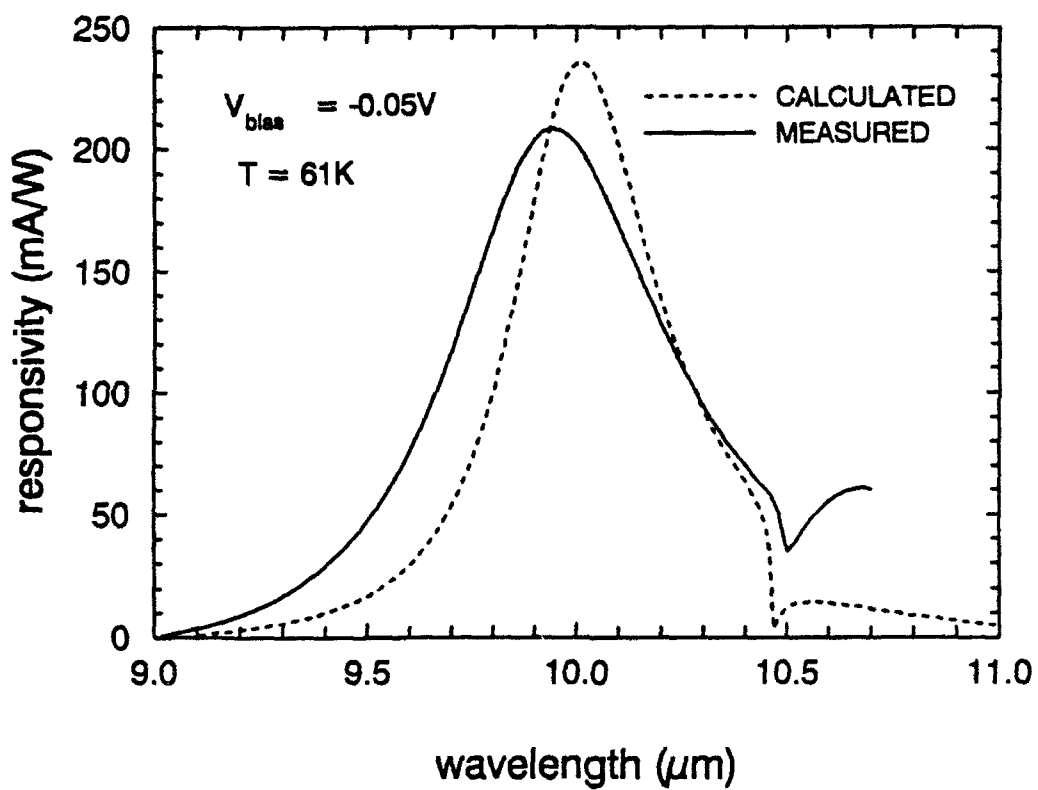


Figure 3.4.3 A comparison of the calculated and measured responsivity vs. wavelength for a square mesh grating coupled InGaAs BTM QWIP.

quantum efficiency may be further improved by using a square mesh grating with $g = 3\mu\text{m}$ and $a = 1.8\mu\text{m}$.

3.5 Geometry Considerations of A 2-D Square Mesh Grating Coupler for A GaAs/AlGaAs QWIP

Summary: The effects of grating size and shape variation on the photoresponse of a 2-D square mesh metal grating coupler for a GaAs/AlGaAs QWIP has been analyzed. In the fabrication of small grating coupler structure on QWIPs, some distortion in the aperture's shape and size may occur during processing. This may lead to nonuniformed photoresponse of cell-to-cell in the QWIP arrays. The effect can be minimized by either selecting a larger aperture size or using a larger grating period.

In an intersubband absorption QWIP, electrons are excited from the bound ground state to a higher level miniband or continuum band by IR radiation, and then transport via the miniband or continuum band states under the applied electric field to produce the photocurrent. The corresponding transitions are allowed only when the electric field component of the incident IR radiation is polarized in the direction of the electron motion. The IR illumination perpendicular to the surface of the QWIP will not be absorbed in type-I QWIPs. Therefore, some special coupling techniques have to be employed, such as using a 45° angle polished facet on one edge of the detectors, Brewster's angle illumination, 1-D lamellar grating and 2-D cross grating. In the 45° polished facet or Brewster's angle illumination coupling, the light can access the detector in only one direction, the coupling is rather weak and not capable of forming a planar image array. In lamellar grating coupling, the FPA is possible but the coupling is polarization dependent. In our design, we use a planar 2-D square mesh metal grating with a conducting screen perforated periodically with square apertures formed on the top contact surface of the detector by standard photolithography and lift-off techniques. The grating scatters the incident IR light into new electromagnetic waves which satisfy the absorption rule described above.

However, fabrication of extremely small grating structure will inevitably introduce cell-to-cell photoresponse nonuniformity in the FPAs, which in turn could introduce spatial noise and limit the sensitivity of IR imaging camera. Since the size of square apertures in the grating is only a few micrometers or smaller, some variation in the width and shape of the grating aperture pattern on a QWIP FPA can be expected. Therefore, the effect of changing the aperture width and shape on the coupling quantum efficiency must be considered in the grating design.

In this section we present a numerical analysis of the effect of grating size and shape variation on the coupling quantum efficiency of a square mesh metal grating coupled GaAs QWIPs. The aperture width is carefully chosen to avoid inducing the uncorrected spatial noise. Finally, a grating scale with good stability was also discussed.

The 2-D square mesh metal grating is deposited on the top surface of a GaAs QWIP as illustrated in Fig. 3.5.1, where a is the aperture width, and g is the grating period. The IR radiation is impinging on the grating under normal incidence conditions. The square apertures are arranged in two orthogonal coordinates \vec{x} and \vec{y} making the whole grating structure as two groups of equally spaced parallel metal lines intersect one another. The unknown electromagnetic waves near the grating are derived by using modal expansion method. Taking wave theory in periodic structure into consideration, we obtain

$$\vec{E}^i = \sum_{r=1}^2 A_{00r} \vec{\Phi}_{00r} \quad (12)$$

where \vec{E}^i is the transverse component of the incident electric field with respect to wave travel direction \hat{z} , $\vec{\Phi}_{00r}$ are the Floquet mode functions, A_{00r} is the corresponding coefficient, and $r = 1$ or 2 is used to designate the TE or TM Floquet modes, respectively. Similarly, the transverse component of the transmitted and reflected electric fields can be written as

$$\begin{aligned} \vec{E}^t &= \sum_p \sum_q \sum_{r=1}^2 B_{pqr} \vec{\Phi}_{pqr} \\ &= \sum_{r=1}^2 A_{00r} \vec{\Phi}_{00r} + \sum_p \sum_q \sum_{r=1}^2 R_{pqr} \vec{\Phi}_{pqr} \end{aligned} \quad (13)$$

where R_{pqr} is the reflection coefficient, and B_{pqr} is the transmission coefficient. Equation (2) also implicitly includes the boundary condition that the tangential electric field vector is continuous in the aperture. Employing the method of moments, these equations are reduced to the following expression

$$[Y_m^M] [F_m] = [I_m] \quad (14)$$

where

$$\begin{aligned} Y_m^M &= \sum_{pq} \sum_{r=1}^2 (\xi_{pqr} + \xi_{pqr}^d) C_{pqr}^{M*} C_{pqr}^m \\ C_{pqr}^m &= \int \int_{\text{aperture}} \vec{\Phi}_{pqr}^* \cdot \vec{\Psi}_m \, du \end{aligned} \quad (15)$$

and

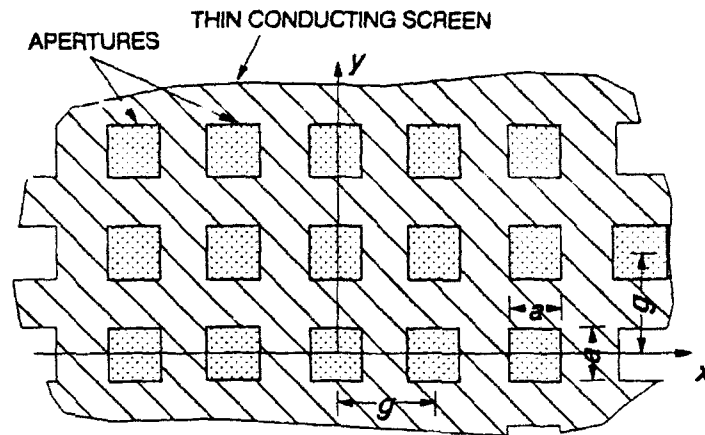
$$I_m = 2 \cdot \sum_{r=1}^2 A_{00r} \xi_{00r}^d C_{00r}^{m*} \quad (16)$$

is the matrix of incidence. The Ψ_m are the waveguide modes spanned by the aperture, F_m is the corresponding expansion coefficient, and ξ_{pqr} and ξ_{pqr}^d are the admittance of the Floquet modes on the two sides of the mesh grating. The integrals C_{pqr}^m are complex numbers and so do the elements of Y_m^M . The coupling efficiency of the grating depends not only on the power of each higher order TM propagating mode but also on the angle enclosed by the electric field vector of the diffracted mode and the free carrier motion vector⁷ \hat{z} , which is denoted by γ

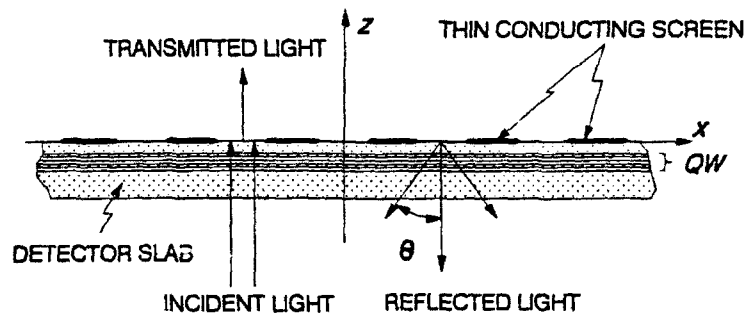
$$\cos \gamma_{pqz} = \frac{\lambda/n_r}{g} \cdot \sqrt{p^2 + q^2} \quad (17)$$

where n_r is the refractive index of the medium in which the wave propagates. Note that the quantum well absorption is directly proportional to the $\cos^2 \gamma$ and the diffracted power. Figure 3.5.2 (a) shows the relative coupling power of the first order diffracted waves as a function of the normalized wavelength for different values of a/g ratio. The second order diffracted waves will not emerge until λ/g is smaller than 2.298 (using $n_r = 3.25$ for GaAs at 77K). Although grating period g remains constant during the photolithography process, the aperture width may be changed or distorted. Figure 3.5.2(b) shows the variation of coupling power of the first order diffracted waves with the normalized aperture width a/g in the most effective coupling regime $2.8 < \lambda/g < 3.2$. The results clearly show that $a/g = 0.6$ is a relatively stable (noncritical) ratio for the aperture width.

The shape of the aperture may be distorted during the fabrication of grating pattern, as shown in Fig.3.5.3(a). In the extreme case, the aperture becomes a circular shape with a radius r equal to half of the square aperture width a , and the grating coupler consists of a conducting screen perforated periodically with circular apertures. The characteristic curve of such a grating is plotted in Fig. 3.5.3(b). Almost invariant coupling curve is obtained for $r/g = 0.3$ to $a/g = 0.6$, which implies that the square mesh metal grating with a normalized aperture width $a/g = 0.6$ is insensitive to the aperture shape even if the pattern is not processed properly. Another approach to reduce the effect of deformation in the grating aperture is to use a larger grating geometry with a lower coupling quantum efficiency. For example, a square mesh grating coupler with $g = 6\mu\text{m}$ and $a = 3\mu\text{m}$ instead of $g = 4\mu\text{m}$, $a = 2\mu\text{m}$ can be used to couple a GaAs/AlGaAs QWIP for 9-11 μm detection. Figure 3.5.4 illustrates the coupling characteristic curves for the 6/3 ratio grating coupler. This larger scale grating has larger aperture size, and hence is easier to fabricate within the same error tolerance limits. Figure 3.5.5(a) and (b) show the calculated optical absorption constants of the first, second and third order diffracted waves, and the calculated coupling quantum efficiency of a GaAs/AlGaAs QWIP using two different sets of grating parameters. The quantum efficiency



(a)



(b)

Figure 3.5.1 (a) Top view of a 2-D square mesh metal grating coupler, (b) side-view showing the incident and transmitted light.

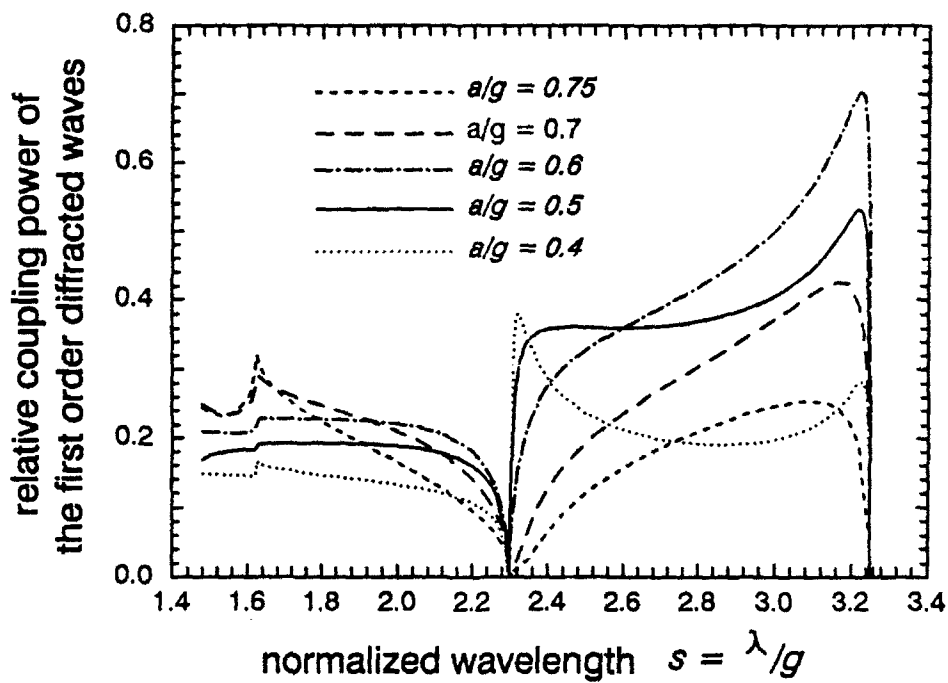


Figure 3.5.2 (a) Relative coupling power of the first order diffracted waves versus normalized wavelength, s , for a 2-D square mesh metal grating coupler, with different ratios of a/g .

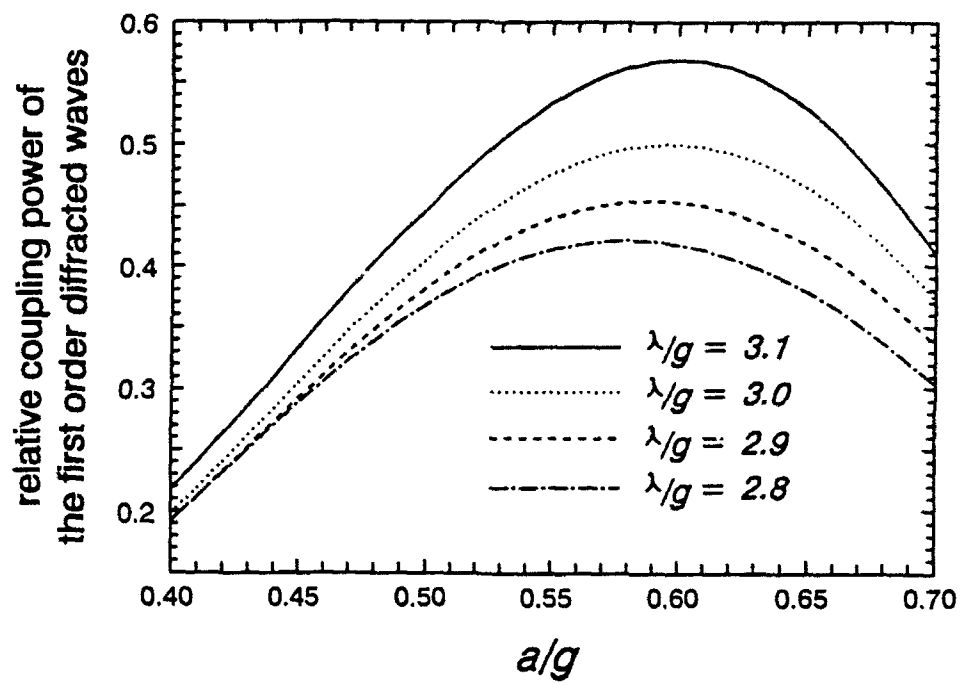


Figure 3.5.2 (b) Relative coupling power of the first order diffracted waves versus normalized aperture width, a/g , for a 2-D square mesh metal grating coupler, with different ratios of λ/g .

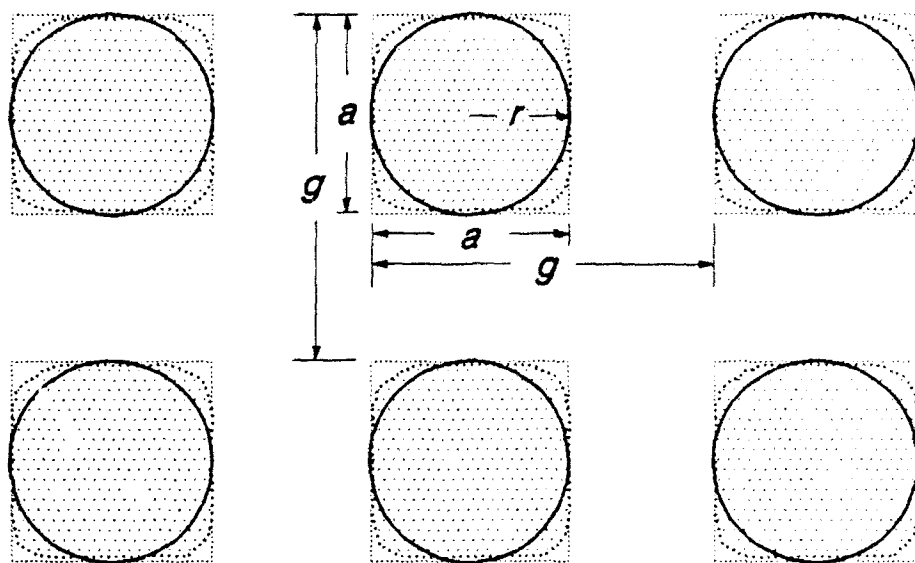


Figure 3.5.3 (a) Top view of the square and circular shape apertures for a 2-D square mesh metal grating coupler.

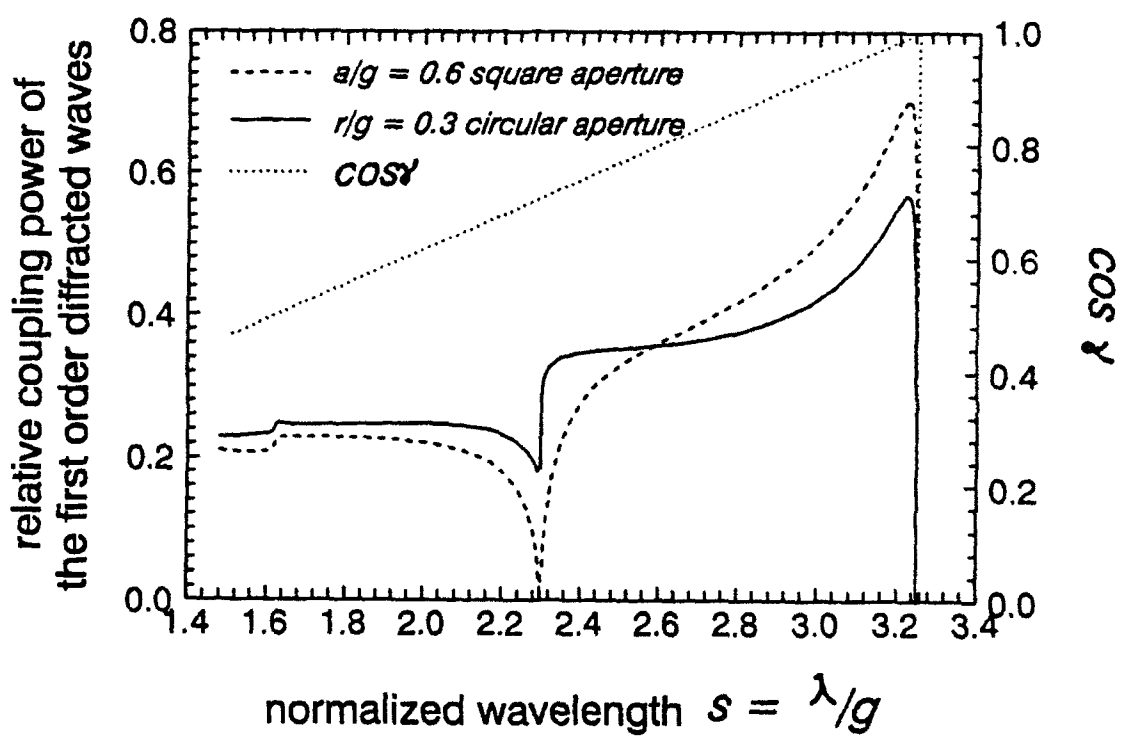


Figure 3.5.3 (b) The relative coupling power of the 1st order diffracted waves vs. normalized wavelength for a square and circular shape aperture.

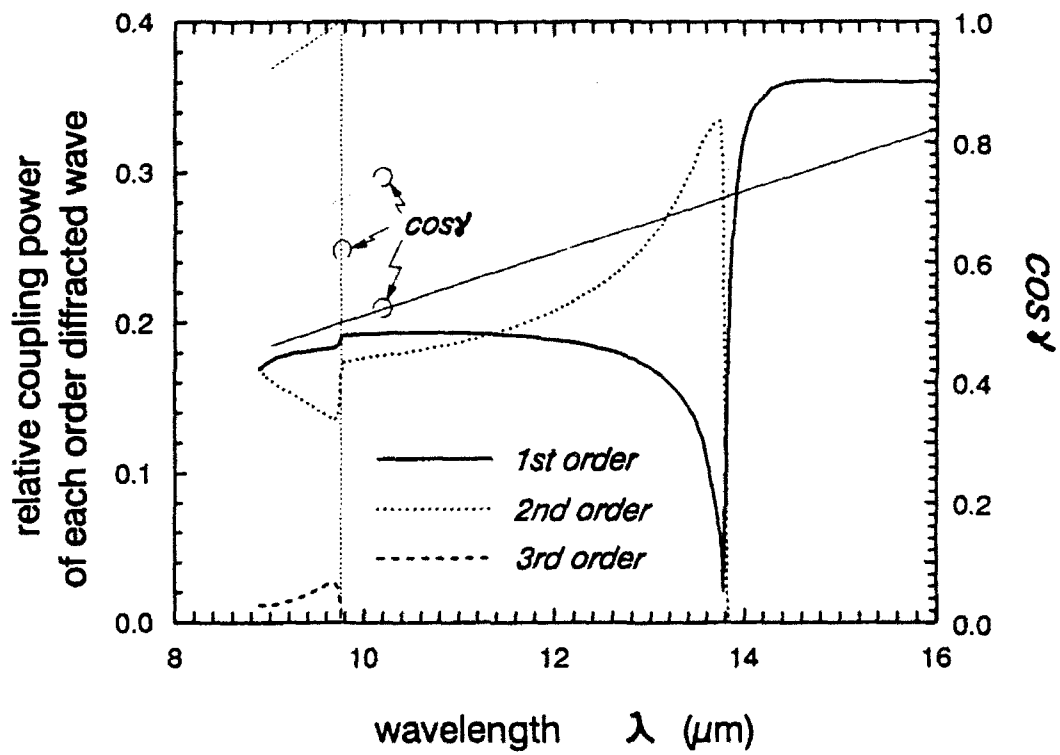


Figure 3.5.4 The relative coupling power of the 1st, 2nd, and 3rd order diffracted waves vs. wavelength for a 2-D square mesh grating coupler with $g = 6 \mu\text{m}$ and $a = 3 \mu\text{m}$.

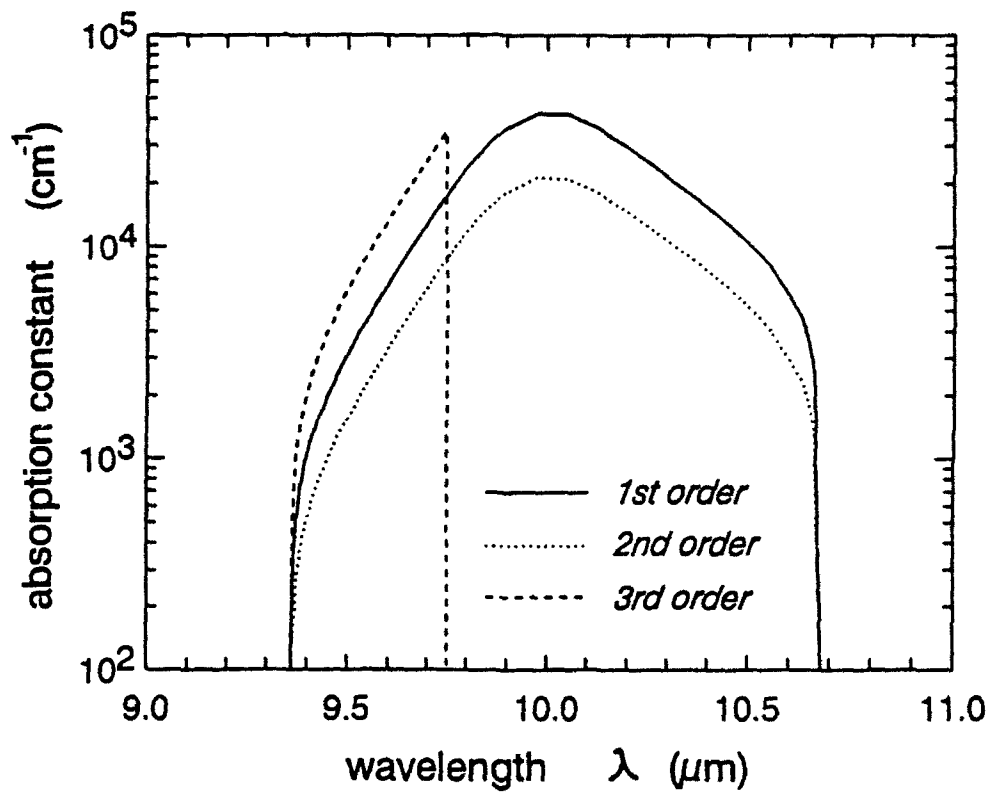


Figure 3.5.5 (a) Optical absorption constant of the 1st, 2nd, and 3rd order diffracted waves vs. wavelength for a 2-D square mesh grating coupled GaAs/AlGaAs QWIP.

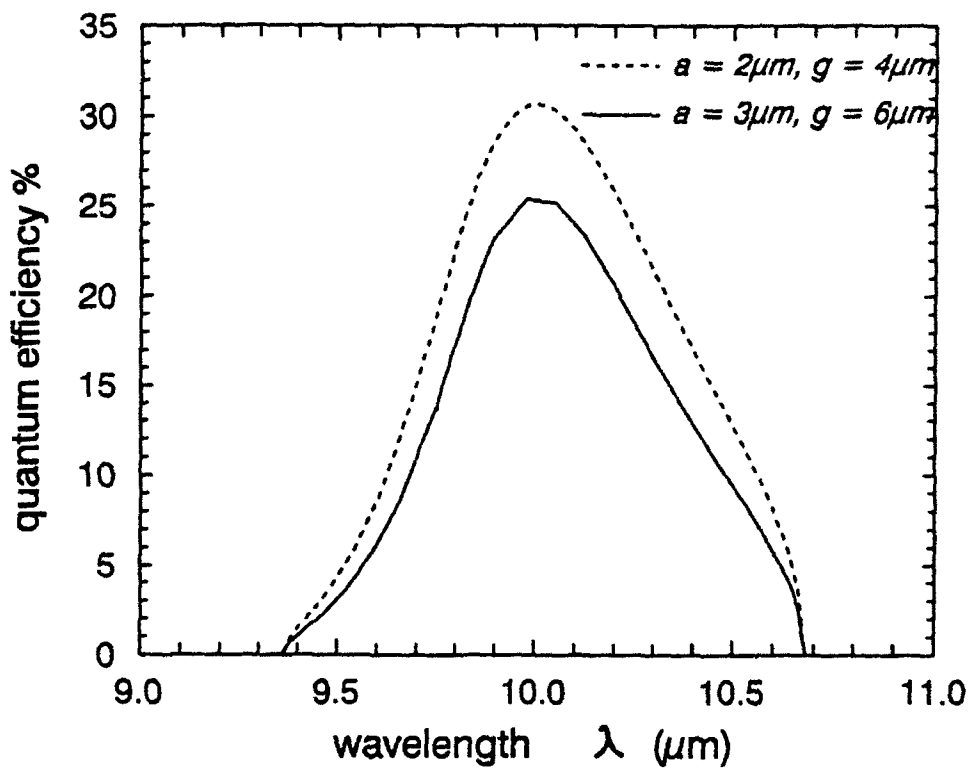


Figure 3.5.5 (b) Coupling quantum efficiency vs. wavelength for a 2-D square mesh grating coupled GaAs/AlGaAs QWIP.

η is calculated by

$$\eta = \mathcal{P}_{eff} \cdot (1 - e^{-\alpha l}) \quad (18)$$

where α is the absorption constant shown in Fig.3.5.5(a), l is the total length of quantum wells (in the present case, $l = (88\text{\AA}) \cdot (40\text{periods}) = 3520\text{\AA}$), and \mathcal{P}_{eff} is the relative coupling power of all the higher order diffracted waves.

In conclusion, the effects of grating shape and grating width variation on the coupling quantum efficiency in a 2-D square mesh metal grating coupled GaAs/AlGaAs QWIP have been analyzed for 8-12 μm detection. It is shown that grating variation generated spatial noise can be reduced either by using noncritical grating geometry or using a larger grating dimension.

3.6 Noise Characterization of An InGaAs/InAlAs BTM QWIP

Summary: Noise characterization for a bound-to-miniband (BTM) transition InGaAs/InAlAs QWIP has been carried out in this work. From measurements of noise spectrum as a function of frequency (10 to 10⁵ Hz), the noise sources in this QWIP were identified. The results revealed that Johnson noise dominated in the low bias voltage region and 1/ f noise dominated in the high bias region. In addition, noise gain versus bias voltage was also determined for this QWIP.

Multiquantum well structures are of great interest because of their novel electronic and optical properties. One of the successful applications of quantum well structures is the use of intersubband transition for long wavelength infrared (IR) detection. In comparison with other IR detectors, like HgCdTe IR detectors, quantum well infrared detectors (QWIPs) have many advantages such as higher yield, lower cost, fewer material defects, and predictable spectral response. To evaluate the performance of a QWIP, detectivity D^* is the most often used figure of merit. In calculating the detectivity at certain frequency, the noise value at this frequency must be known. Another important parameter for evaluating the QWIP performance is the dark current noise gain. The noise associated with the dark current of a QWIP is usually controlled by trapping and detrapping processes at the quantum well/barrier layer interface, and is generation-recombination (g-r) in nature. In this respect, the noise gain can be calculated from noise spectrum. Therefore, the noise measurements are necessary in evaluating the performance of the QWIPs. In this section, we present the measurements on noise spectrum in a bound-to-miniband (BTM) transition in InGaAs/InAlAs QWIP at 77 K.

1. Johnson Noise:

Let us consider the case given as follow: the number of events per second is the number of random collisions per second. The contribution per event is the fractional charge given by $e\frac{l}{L}$, where l is the mean free path between collisions. Using one-dimensional argument, the mean-square noise current becomes

$$I_n^2 = 2\frac{N}{\tau_c} \left(e\frac{l}{L} \right)^2 \Delta B \quad (19)$$

where, N is the total number of photoexcited carriers, and $l = v\tau_c$. Since $1/2mv^2 = 1/2kT$ and $\tau_c e/m = \mu$, l^2 can be written as

$$l^2 = (v\tau_c)^2 = 2kT\frac{\mu}{e}\tau_c \quad (20)$$

With $eN\mu/L^2 = 1/R$, the mean-square noise current per unit bandwidth is given by

$$\begin{aligned} I_n^2 &= 4\frac{Nev}{L^2} kT\Delta B \\ &= 4\frac{kT}{R}\Delta B \end{aligned} \quad (21)$$

2. Generation-Recombination Noise

From the traditional analysis of g-r noise, the creation and annihilation of free carriers in semiconductor device may be described by

$$\frac{d\Delta N}{dt} = -\frac{\Delta N}{\tau} + H(t) \quad (22)$$

where ΔN is the fluctuation in the number of carriers, τ is the life time of excess carriers, and $H(t)$ is the random noise term.

Using Fourier transformation, we can obtain

$$S_N(f) = \frac{S_H(0)\tau^2}{1 + \omega^2\tau^2} \quad (23)$$

with

$$\overline{\Delta N^2} = \int_0^\infty S_N(f)df = S_H(0)\tau \int_0^\infty \frac{\tau df}{1 + \omega^2\tau^2} = \frac{S_H(0)\tau}{4}$$

so that

$$S_N(f) = 4\overline{\Delta N^2} \frac{\tau}{1 + \omega^2\tau^2} \quad (24)$$

Assuming the number of total carriers is N_c and the current caused by one electron is i_e , we have $\bar{I} = i_e N_c$. Thus,

$$S_i(f) = i_e^2 S_N(f) = 4i_e^2 \overline{\Delta N^2} \frac{\tau}{1 + \omega^2\tau^2} = 4\bar{I}^2 \frac{\overline{\Delta N^2}}{N_c^2} \frac{\tau}{1 + \omega^2\tau^2}$$

For majority carrier device, $\overline{\Delta N^2}$ is equal to N_c . In a QWIP, the average number of conduction electron is equal to the total number of carriers excited. Using $\bar{I} = \frac{eN_c}{\tau_d}$ (where τ_d is the carrier transport time), we obtain

$$S_i(f) = 4\bar{I}^2 \frac{1}{N_c} \frac{\tau}{1 + \omega^2 \tau^2} = 4e\bar{I} \frac{\frac{\tau}{\tau_d}}{1 + \omega^2 \tau^2} \quad (25)$$

where $g = \frac{\tau}{\tau_d}$ is defined as "noise gain" in a QWIP.

In our case, $\omega\tau \ll 1$, the g-r noise spectrum can be simplified to

$$S_i \approx 4e\bar{I}g \quad (26)$$

Therefore, the noise spectrum due to g-r noise of a QWIP is constant in the frequency domain.

Figure 3.6.1 shows the dark current and differential resistance versus bias voltage for an InGaAs/InAlAs BTM QWIP. In our measurements, eighteen data points were taken between -1 V to +1 V. The frequency range for each data point is from 10 Hz to 100 KHz.

The characteristic noise density spectra are plotted in Fig.3.6.2 (a) and (b) for bias voltages, $V_b = -0.083, -0.453, \text{ and } -1.06$ V, respectively. The strong signal appears at 10Hz to 100Hz in the noise spectrum was believed to be the stray noise picking up during the measurements (e.g. 60Hz power line signal) and should be ignored. By selecting the right g-r noise density, $S_i(f)$, the noise density versus reversed bias voltage is shown in Fig 3.6.3.

From the measured results, it is seen that Johnson noise is the dominate noise source at low bias region. Once the applied voltage increases (under both forward bias and reverse bias over 0.06 V), the g-r noise becomes dominant. Under the condition, $\omega\tau \ll 1$, the noise gain can be calculated by using $g = \frac{S_i - S_{i,Johnson}}{4e\bar{I}}$. We use $S_{i,Johnson} = 2.0 \times 10^{-24} A^2/Hz$ from the measured data. Figure 3.6.4 shows the noise gain as a function of applied bias for the InGaAs BTM QWIP. Large noise gain factor was observed in this QWIP.

In general, it is not desirable to operate the detector at $1/f$ noise dominant region. From our noise measurements, we found that the available operation bias is -0.07 V to -1 V and 0.07 V to 0.15 V. There is no doubt that operation under reverse bias is much better than the forward bias for the BTM QWIP. This result is good agreement with the InGaAs SBTM QWIP reported previously. In general, BTM transition QWIP structure is expected to be less noisy than the standard QWIP due to the lower dark current in this device. It has been shown that the dark current and noise gain

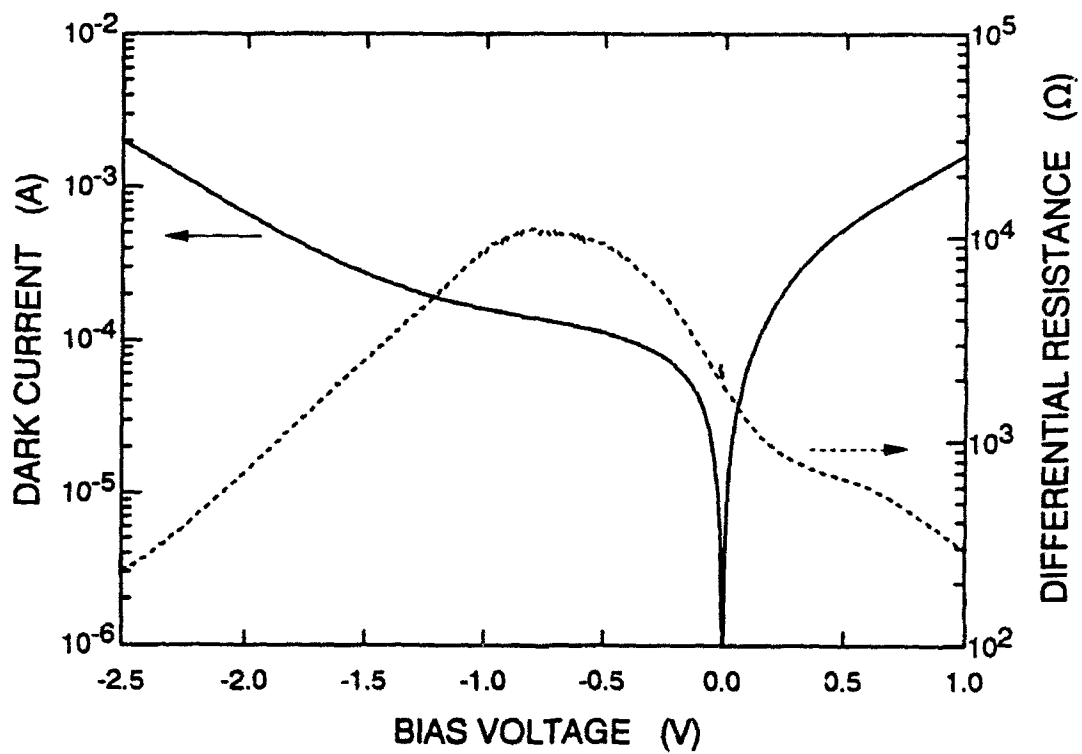


Figure 3.6.1 Darkcurrent and differential resistance vs. bias voltage for an InGaAs/InAlAs BTM QWIP measured at 77 K.

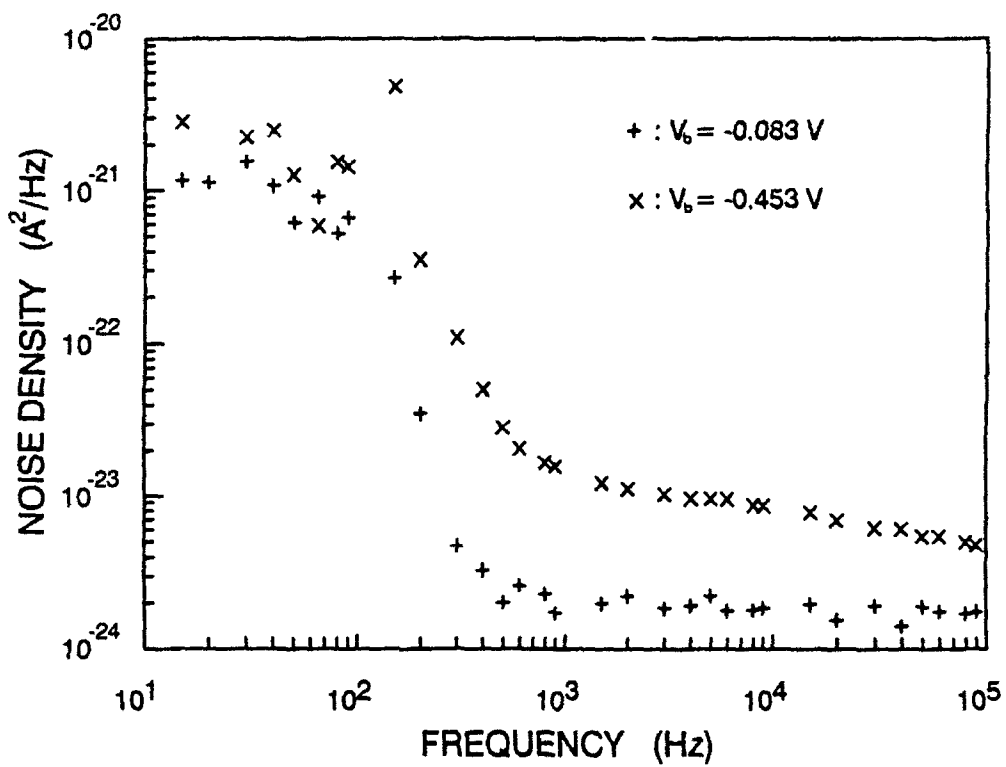


Figure 3.6.2 Noise density versus frequency for an InGaAs BTM QWIP measured at $V_b = -0.083, -0.453$ V.

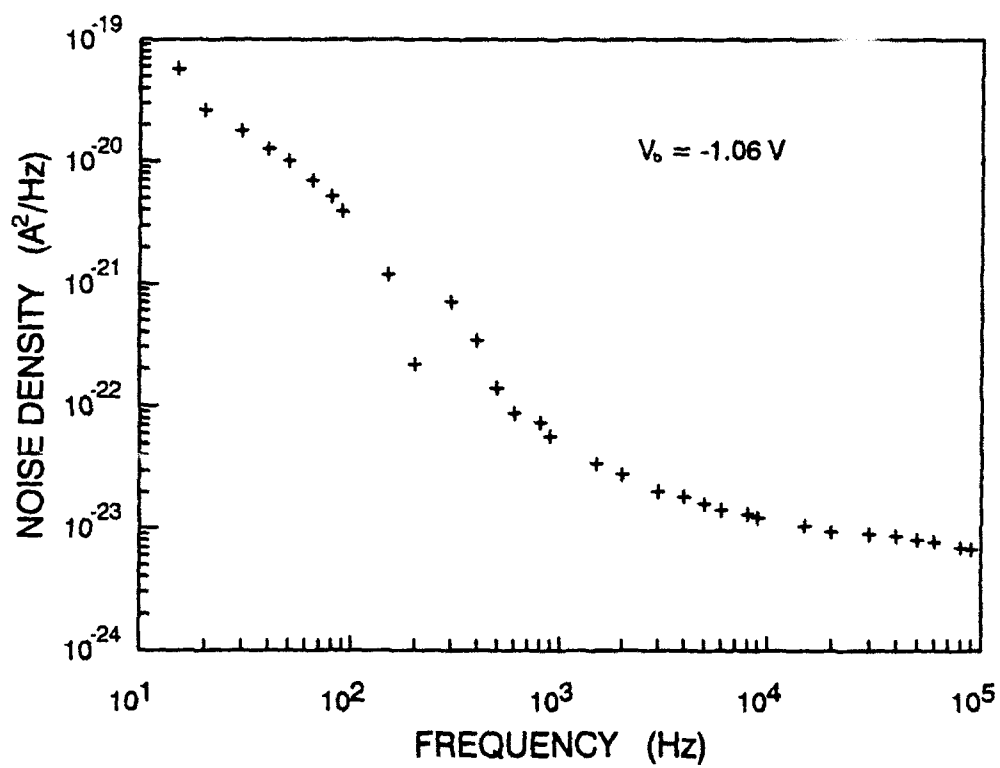


Figure 3.6.2 (b) Noise density versus frequency for an InGaAs BTM QWIP measured at $V_b = -1.06$ V, showing $1/f$ noise dominant at low frequency regime.

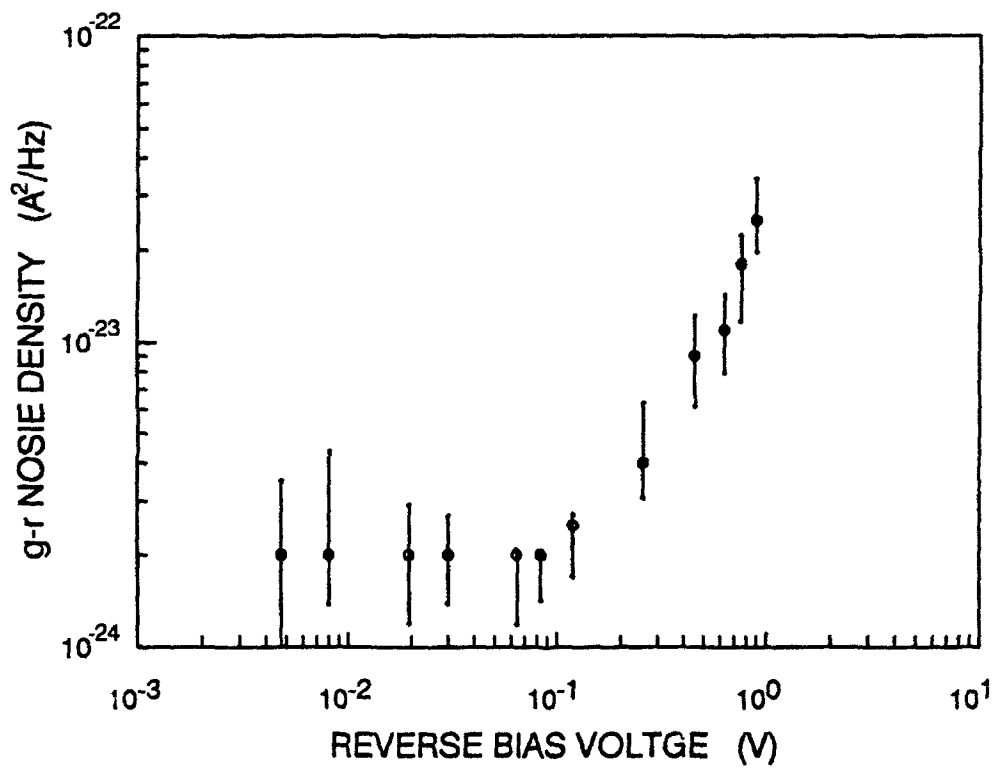


Figure 3.6.3 g-r noise density versus reverse bias voltage for an InGaAs BTM QWIP, Johnson noise is dominant for $V_b < 0.1$ V.

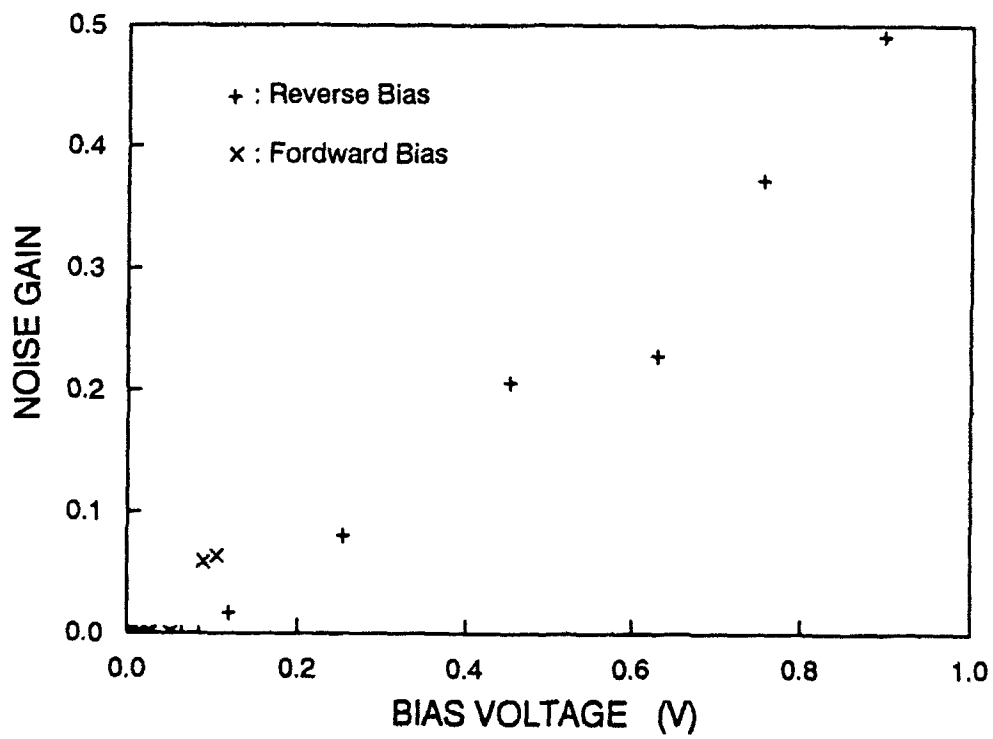


Figure 3.6.4 Noise gain versus bias voltage for an InGaAs BTM QWIP.

are strongly related in the conventional QWIP. To further study the noise origins in the QWIP devices, we plan to perform measurements of the noise spectrum on other types of QWIPs, and the results will be reported in the next quarterly progress report.

3.7 References

1. B. F. Levine, R. J. Malik, J. Walker, K. K. Choi, C. G. Bethea, D. A. Kleinman, and J. M. Vandenberg, *Appl. Phys. Lett.* **50**, 273 (1987).
2. L. S. Yu, S. S. Li, *Appl. Phys. Lett.* **59**, 1332 (1991).
3. Y. C. Chang, R. B. James, *Phys. Rev.* **B-39**, 12672 (1989).
4. B. F. Levine, S. D. Gunapala, J. M. Kuo, S. S. Pei, and S. Hui, *Appl. Phys. Lett.* **59**, 1864 (1991).
5. J. Katz, Y. Zhang, and W. I. Wang, *Electron. Lett.* **28**, 932 (1992).
6. W. S. Hobson, A. Zussman, B. F. Levine, and J. deJong, *J. Appl. Phys.* **71**, 3642 (1992).
7. H. Xie, J. Katz, and W. I. Wang, *Appl. Phys. Lett.* **59**, 3601 (1991).
8. H. Asai, and Y. Kawamura, *Appl. Phys. Lett.* **56**, 746 (1990).
9. B. F. Levine, K. K. Choi, C. G. Bethea, J. Walker, and R. J. Malik, *Appl. Phys. Lett.* **50**, 1092 (1987).
10. T. S. Faska, J. W. Little, W. A. Beck, K. J. Ritter, A. C. Goldberg, and R. LeBlanc. *Innovative Infrared Photodetector Workshop, JPL, Pasadena, April 7-9, 1992.*
11. J. D. Ralston, H. Schneider, D. F. Gallagher, K. K. Fuchs, P. Bittner, B. Dischler, and P. Koidl, *J. Vac. Sci. Technol.* **B**, 998 (1992).
12. B. F. Levine, C. G. Bethea, G. Hasnain, V. O. Shen, E. Pelve, R. R. Abbott, and S. J. Hsieh, *Appl. Phys. Lett.* **56**, 851 (1990).
13. G. Hasnain, B. F. Levine, D. L. Sivco, and A. Y. Cho, *Appl. Phys. Lett.* **56**, 770 (1990).
14. K. W. Goossen, S. A. Lyon, and K. Alavi, *Appl. Phys. Lett.* **52**, 1701 (1988).
15. B. F. Levine, S. D. Gunapala, and R. F. Kopf, *Appl. Phys. Lett.* **58**, 1551 (1991).

16. C. S. Wu, C. P. Wen, R. N. Sato, M. Hu, C. W. Tu, J. Zhang, L. D. Flesner, L. Pham, and P. S. Nayer, *IEEE Trans.* **ED-39**, 234 (1992).
17. H. Schnelder, K. Kheng, M. Rainsteiner, J. D. Ralston, F. Fuchs, and P. Koidl, *Appl. Phys. Lett.* **60**, 1471 (1992).
18. L. S. Yu, Sheng S. Li, and Pin Ho, *Electron. Lett.* **28**, 1468 (1992).
19. P. Dawson, B. A. Wilson, C. W. Tu, and R. C. Miller, *Appl. Phys. Lett.* **48**, 541 (1986).
20. K. K. Choi, B. F. Levine, C. G. Bethea, J. Walker, and R. J. Malik, *Appl. Phys. Lett.* **50**, 1814; **52**, 1979 (1988).
21. E. R. Brown and S. J. Eglash, *Phys. Rev.* **41**, 7559 (1990).
22. P. Lefebvre, B. Gil, H. Mathieu, and R. Planel, *Phys. Rev.* **39**, 5550 (1989).
23. M. Dabbicco, R. Cingolani, M. Ferrara, K. Ploog, and A. Fischer, *Appl. Phys. Lett.* **59**, 1497 (1991).
24. J. Katz, Y. Zhang, and W. I. Wang, *Appl. Phys. Letts.*, **61**, 1697 (1992).
25. Pin Ho and P. A. Martin, L. S. Yu, Y. H. Wang, and S. S. Li, *J. Vacuum. Science Technol.* Oct. (1992).
26. M. Dabbicco, R. Cingolani, M. Ferrara, L. Tapfer, A. Fischer, and K. Ploog, *J. Appl. Phys.* **72**, 1512 (1992)
27. E. O. Kane, *J. Phys. Chem. Solid I*, 249 (1957).
28. L. I. Schiff, *Quantum Mechanics* (McGraw-Hill, New York, 1968).
29. E. Haga and H. Kimura, *J. Phys. Soc. Jpn.* **18**, 777 (1963).
30. F. Stern and W. E. Howard, *Phys. Rev.* **163**, 816 (1967).
31. C. L. Yang, D. S. Pan, and R. Somoano, *J. Appl. Phys.* **65**, 3253 (1989).
32. Y. H. Wang, S. S. Li, and Pin Ho, *Appl. Phys. Lett.* **62**, 93 (1993).
33. M. Dutta, H. Shen, D. D. Smith, K. K. Choi, and P. G. Newman, *Surface Science*, **267**, 474 (1992).

34. D. Z. Y. Ting and T. C. McGill, *J. Vac. Sci. Technol. B* **10**, 1980 (1992).
35. B. F. Levine, S. D. Gunapala, and R. F. Kopf, *Appl. Phys. Lett.* **58**, 1551 (1991)
36. H. C. Liu, *Appl. Phys. Lett.* **51**, 1019 (1987).
37. J. Feldmann, E. Gobel, and K. Ploog, *Appl. Phys. Lett.* **57**, 1520 (1990).
38. Y. H. Wang, Sheng S. Li, and Pin Ho, *Appl. Phys. Lett.* **62**, 621 (1993).
39. W. S. Fu, G. R. Olbright, J. F. Klem, and J. S. Harris Jr., *Appl. Phys. Lett.* **61**, 1661 (1992).
40. B. F. Levine, K. K. Choi, C. G. Bethea, J. Walker, and R. J. Malik, *Appl. Phys. Lett.* **50**, 1092 (1987).
41. B. F. Levine, C. G. Bethea, G. Hasnian, V. O. Shen, E. Pelve, and P. R. Abbott, *Appl. Phys. Lett.* **56**, 851 (1990).
42. L. C. West and S. J. Eglash, *Appl. Phys. Lett.* **46**, 1156 (1985).
43. J. Y. Andersson, L. Lundqvist, and Z. F. Paska, *Appl. Phys. Lett.* **58**, 2264 (1991).
44. K. W. Goossen and S. A. Lyon, *Appl. Phys. Lett.* **47**, 1257 (1985).
45. J. Y. Andersson, L. Lundqvist, and Z. F. Paska, *Appl. Phys. Lett.* **59**, 857 (1991).
46. C. C. Chen, *IEEE MTT-18*, 627 (1970).
47. D. D. Coon, R. P. G. Karunasiri, and L. Z. Liu, *Appl. Phys. Lett.* **47**, 289 (1985).
48. I. Gravé, A. Shakouri, N. Kuze, and A. Yariv, *Appl. Phys. Lett.*, **60**, 2362 (1992).
49. A. Köck, E. Gornik, G. Abstreiter, G. Böhm, M. Walther, and G. Weimann, *Appl. Phys. Lett.* **60**, 2011 (1992).
50. E. Martinet, F. Luc, E. Rosencher, Ph. Bois, and S. Delaitre, *Appl. Phys. Lett.* **60**, 895 (1992).
51. W. J. Li, B. D. McCombe, F. A. Chamber, G. P. Devane, J. Ralston, and G. Wicks, *Surf. Sci.* **228**, 164 (1990).
52. M. J. Kane, M. T. Emeny, N. Apsley, C. R. Whitehouse and D. Lee *Semicond. Sci. Technol.* **3**, 722 (1988).

53. C. G. Bethea, B. F. Levine, et. al., IEEE Trans. ED-38, 1118 (1991).
54. Z. Ikonić, V. Milanović, D. Tjapkin, Appl. Phys. Lett. 54, 247(1989).
55. G. Hasnain, B. F. Levin, C. G. Bethea, R. A. Logan, J. Walker, and R. J. Malik, Appl. Phys. Lett. 54, 2515 (1989).
56. J. M. Mooney, F. D. Shepherd, W. S. Ewing, J. E. Murguire, and J. Silverman. Opt. Eng. 28, 1151 (1989).
57. J. Y. Andersson and L. Lundqvist, J. Appl. Phys. 71, 3600 (1992).
58. C. C. Chen, IEEE Trans MTT-18, 627 (1970).
59. B. F. Levine, C. G. Bethea, G. Hasnain, J. Walker, and R. J. Malik, Appl. Phys. Lett. 53 296 (1988).
60. B. F. Levine, G. Hasnain, C. G. Bethea, and N. Chand, Appl. Phys. Lett. 54, 2704 (1989).
61. L. S. Yu, Y. H. Wang, Sheng S. Li, and Pin Ho, Appl. Phys. Lett. 60, 992 (1992).
62. L. S. Yu, Sheng S. Li, Y. H. Wang, and Y. C. Kao, J. Appl. Phys. 72, 2105 (1992).
63. Y. H. Wang, Sheng S. Li, Appl. Phys, Lett. 62, 621 (1993)
64. A. Zussman, B. F. Levine, J. M. Kuo, and J. de Jong, J. Appl. Phys. 70, 5101 (1991).
65. B. F. Levine, A. Zussman, S. D. Gunapala, M. T. Asom, J. M. Kuo, and W. S. Hobson, J. Appl. Phys. 72 4429 (1992).
66. H. C. Liu, Appl. Phys. Lett. 61 2703 (1992).
67. Albert Rose, *Concepts in Photoconductivity and Allied Problems*, edited by R. E. Marshak (Wiley-Interscience, New York, 1963), p. 97-108.
68. Aldert van der Ziel, *Noise in Solid State Devices and Circuits*, p.18-23 Wiley-Interscience, New York, 1986.